14 The Dynamic Cluster Approximation and its DCA$^+$ Extension

Thomas A. Maier
Computer Science and Mathematics Division
Center for Nanophase Materials Sciences
Oak Ridge National Laboratory

Contents

E. Pavarini, E. Koch, and P. Coleman (eds.)
Many-Body Physics: From Kondo to Hubbard
Modeling and Simulation Vol. 5
Forschungszentrum Jülich, 2015, ISBN 978-3-95806-074-6
http://www.cond-mat.de/events/correl15

1 Introduction

Theoretical studies of materials governed by strong electronic interactions remain one of the most challenging problems in condensed matter physics. While the Schrödinger equation describing these systems is known, the complexity of its solution increases exponentially with the number of electrons so that approximations have to be made. Mainstream theoretical modeling based on density-functional theory attempts to solve the full equation by mapping the many-body problem onto a single-particle problem. But its implementation in terms of the local density approximation fails to account for the strong correlations between the electrons and thus is unsuccessful in describing many of the many-body phenomena in these systems, such as magnetism or superconductivity. To study such behavior, a different approach is usually employed in order to make the problem tractable: A simplified model Hamiltonian is devised to provide an accurate description of the important low-energy degrees of freedom and higher energy states are left out. Because of this reduction in complexity, the model can then be solved with accurate many-body methods that treat the interactions accurately and thus are able to describe phenomena due to strong electronic correlations. Much of the work in this area is based on using methods such as exact diagonalization or quantum Monte Carlo (QMC) to determine the exact state of a finite-size lattice and regarding this state as an approximation to the bulk thermodynamic limit. Quantum cluster methods [1] such as the dynamic cluster approximation (DCA) [2–4], the subject of this lecture, use a different philosophy, in which the bulk, infinite-size, lattice problem is replaced by a finite-size cluster embedded in a mean-field bath designed to represent the remaining degrees of freedom. In contrast to finite-size calculations, quantum cluster methods give approximate results for the thermodynamic limit. They have been used extensively since their initial development in 1988 [2] and have provided insight into many important questions of condensed matter science. In this lecture, we present a pedagogical discussion of the DCA framework and its recent DCA$^+$ extension [5, 6], together with selected applications that showcase the ability of these methods to provide insight into the physics of strongly correlated systems.

Preliminaries

In general, the Hamiltonian describing the physics of an interacting system is divided into a non-interacting part H_0 and an interacting part H_1

$$H = H_0 + H_{\rm int}\,. \tag{1}$$

As a simple example, we will focus one of the most studied models in this field, the single-band Hubbard model [7]

$$H = \sum_{ij,\sigma} t_{ij}\, c^\dagger_{i\sigma} c_{j\sigma} + U \sum_i n_{i\uparrow} n_{i\downarrow}\,. \tag{2}$$

Here $c^{(\dagger)}_{i\sigma}$ destroys (creates) an electron on site i with spin σ, and $n_{i\sigma} = c^\dagger_{i\sigma} c_{i\sigma}$ is the corresponding number operator. The first (non-interacting) term describes the hopping of electrons

between sites i and j with amplitude t_{ij}, and the second (interaction) term raises the energy by the Coulomb repulsion U when two electrons with opposite spin reside on the same site.
The single-particle dynamics of the Hamiltonian at finite temperatures is described by the thermodynamic Green's function

$$G_{ij,\sigma} = -\langle T_\tau \, c_{i\sigma}(\tau) c^\dagger_{j\sigma} \rangle \,, \tag{3}$$

$$G_{ij,\sigma}(i\omega_n) = \int_0^\beta d\tau \, e^{i\omega_n \tau} G_{ij,\sigma}(\tau) \,, \;\; \omega_n = (2n+1)\pi/\beta \,, \tag{4}$$

$$G_\sigma(\boldsymbol{k}, i\omega_n) = \frac{1}{N} \sum_{ij} e^{i\boldsymbol{k}(\boldsymbol{r}_i - \boldsymbol{r}_j)} G_{ij,\sigma}(i\omega_n) \,. \tag{5}$$

Here τ is the imaginary time, T_τ the time-ordering operator, $\beta = 1/T$ the inverse temperature, and ω_n are the fermionic Matsubara frequencies. For problems with translational symmetry in space and time, the Green's function becomes diagonal in momentum $\boldsymbol{k}$ and frequency $i\omega_n$ as stated in Eqs. (4) and (5). The Green's function G_0 of the non-interacting system, i.e. $H = H_0$, is given by

$$G_0(\boldsymbol{k}, i\omega_n) = \frac{1}{i\omega_n + \mu - \varepsilon_{\boldsymbol{k}}} \,, \tag{6}$$

where μ is the chemical potential and $\varepsilon_{\boldsymbol{k}}$ the dispersion, obtained from a Fourier transform of the hopping t_{ij}. For example, for a two-dimensional (2D) model with nearest neighbor hopping t and next-nearest-neighbor hopping t', one has

$$\varepsilon_{\boldsymbol{k}} = -2t(\cos k_x + \cos k_y) - 4t' \cos k_x \cos k_y \tag{7}$$

with $\boldsymbol{k} = (k_x, k_y)$. Finally, the Dyson equation

$$G(\boldsymbol{k}, i\omega_n) = \frac{1}{G_0^{-1}(\boldsymbol{k}, i\omega_n) - \Sigma(\boldsymbol{k}, i\omega_n)} \,. \tag{8}$$

defines the self-energy $\Sigma(\boldsymbol{k}, i\omega_n)$ as the difference between the (inverse) non-interacting Green's function G_0 and the fully renormalized Green's function G and thus describes the effects of the interaction term H_{int} on the single-particle dynamics.

2 The dynamic cluster approximation

Calculating the Green's function G and the self-energy Σ exactly in the thermodynamic limit is prohibitively expensive as the problem size grows exponentially in the number of degrees of freedom. Finite-size methods, such as determinantal QMC [8] or Lanczos diagonalization [9], make the problem tractable by restricting the sums over sites in Eq. (2) to those of a finite size $L \times L$ cluster, small enough to be able to calculate the Green's function of the cluster, $G_c(\boldsymbol{K}, i\omega_n)$, and the cluster self-energy $\Sigma_c(\boldsymbol{K}, i\omega_n)$, where $\boldsymbol{K}$ are the momenta of the finite-size cluster. Then, one could imagine carrying out calculations on a set of $L \times L$ lattices and then scaling to the thermodynamic limit $L \to \infty$. The DCA [1–3] takes a different approach: Similar to a finite-size calculation, it represents the system by a reduced number of cluster degrees of

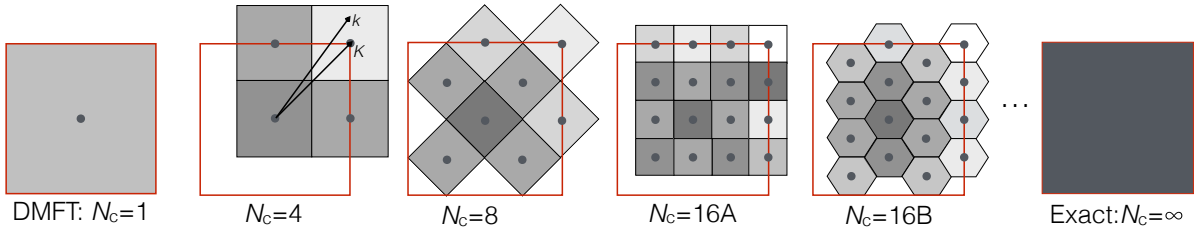

Fig. 1: Coarse-graining of momentum space: *At the heart of the DCA method is a partitioning of the first Brillouin zone into N_c patches over which the Green's function is coarse-grained (averaged) to represent the system by a reduced number of N_c "cluster" degrees of freedom. The bulk degrees of freedom not included on the cluster are taken into account as a mean-field. For $N_c = 1$, the dynamical mean-field approximation is recovered, while for $N_c \to \infty$, one obtains the exact result. For a given cluster size N_c, one can have different locations and shapes of the coarse-graining patches, as illustrated for N_c =16A and 16B.*

freedom, but instead uses coarse-graining to retain information about the degrees of freedom not contained in the cluster. In the Appendix, we provide a rigorous derivation of both the DCA and DCA$^+$ algorithms based on approximations of the grand potential. In the following, we give a more physically motivated discussion of these algorithms.

2.1 General formalism

To coarse-grain the degrees of freedom, the Brillouin zone is split into N_c patches of equal size. As illustrated in Fig. 1, each patch is represented by the cluster momentum $\boldsymbol{K}$ at the center of the cell, and a patch function

$$\phi_{\boldsymbol{K}}(\boldsymbol{k}) = \begin{cases} 1, & \text{if } \boldsymbol{k} \text{ in patch } \boldsymbol{K}. \\ 0, & \text{otherwise.} \end{cases} \tag{9}$$

is used to restrict momentum sums over momenta $\boldsymbol{k}$ inside the $\boldsymbol{K}^{th}$ patch. There can be different numbers N_c of patches, with different size and shape. The basic assumption of the DCA then is that the self-energy is only weakly momentum dependent, so it can be approximated on a coarse grid of $\boldsymbol{K}$-points of a finite-size cluster

$$\Sigma(\boldsymbol{k}, i\omega_n) \simeq \Sigma_c(\boldsymbol{K}, i\omega_n)\,. \tag{10}$$

Since the self-energy describes energy shift and life-time effects due to the interaction of an electron with other electrons, the dynamics of which is represented by the Green's function $G(\boldsymbol{k}, i\omega_n)$, it is generally a functional of $G(\boldsymbol{k}, i\omega_n)$, i.e., $\Sigma(\boldsymbol{k}, i\omega_n) = \Sigma[G(\boldsymbol{k}, i\omega_n)]$. In finite-size methods, the degrees of freedom are reduced to those of a cluster by calculating the self-energy from the cluster Green's function, i.e., $\Sigma_c(\boldsymbol{K}, i\omega_n) = \Sigma_c[G_c(\boldsymbol{K}, i\omega_n)]$. In contrast, in the DCA, all the degrees of freedom of the bulk lattice are retained by calculating the self-energy

$\Sigma_c(\boldsymbol{K}, i\omega_n) = \Sigma_c[\bar{G}(\boldsymbol{K}, i\omega_n)]$ from a coarse-grained Green's function

$$\bar{G}(\boldsymbol{K}, i\omega_n) = \frac{N_c}{N} \sum_{\boldsymbol{k}} \phi_{\boldsymbol{K}}(\boldsymbol{k})\, G(\boldsymbol{k}, i\omega_n) = \frac{N_c}{N} \sum_{\boldsymbol{k}} \phi_{\boldsymbol{K}}(\boldsymbol{k})\, \frac{1}{i\omega_n - \varepsilon_{\boldsymbol{k}} + \mu - \Sigma^{DCA}(\boldsymbol{k}, i\omega_n)}\,. \tag{11}$$

Here the patch function $\phi_{\boldsymbol{K}}(\boldsymbol{k})$ restricts the sum to momenta $\boldsymbol{k}$ inside the $\boldsymbol{K}^{th}$ patch and the DCA self-energy

$$\Sigma^{DCA}(\boldsymbol{k}, i\omega_n) = \sum_{\boldsymbol{K}} \phi_{\boldsymbol{K}}(\boldsymbol{k}) \Sigma_c(\boldsymbol{K}, i\omega_n) \tag{12}$$

is approximated by a constant self-energy $\Sigma_c(\boldsymbol{K}, i\omega_n)$ within the $\boldsymbol{K}^{th}$ patch, but varies between patches. $\bar{G}(\boldsymbol{K}, i\omega_n)$ represents a Green's function in which the degrees of freedom not contained on the cluster are coarse-grained or averaged out. The corresponding non-interacting Green's function

$$\mathcal{G}_0(\boldsymbol{K}, i\omega_n) = \left[\bar{G}^{-1}(\boldsymbol{K}, i\omega_n) + \Sigma_c(\boldsymbol{K}, i\omega_n)\right]^{-1} \tag{13}$$

is obtained by removing the cluster self-energy $\Sigma_c(\boldsymbol{K}, i\omega_n)$. To calculate $\Sigma_c(\boldsymbol{K}, i\omega_n)$, an effective cluster model is set up using $\mathcal{G}_0$ together with the interaction term $H_{\rm int}$ of the Hamiltonian Eq. (2),

$$S[\phi^*, \phi] = -\int_0^\beta d\tau \int_0^\beta d\tau' \sum_{ij,\sigma} \phi^*_{i\sigma}(\tau)\, \mathcal{G}_{0,ij,\sigma}(\tau - \tau')\, \phi_{j\sigma}(\tau) + \int_0^\beta d\tau \sum_i U \phi^*_{i\uparrow}(\tau)\phi_{i\uparrow}\phi^*_{i\downarrow}(\tau)\phi_{i\downarrow}(\tau)\,, \tag{14}$$

where ϕ and ϕ^* are the Grassmann variables corresponding to the operators c and $c^\dagger$, respectively. From this the cluster Green's function

$$G_{c,ij,\sigma}(\tau - \tau') = \frac{1}{Z} \int \mathcal{D}[\phi^*\phi]\, \phi_{i\sigma}(\tau)\phi^*_{j\sigma}(\tau')\, e^{-S[\phi^*,\phi]}\,, \tag{15}$$

where

$$Z = \int \mathcal{D}[\phi^*\phi]\, e^{-S[\phi^*,\phi]} \tag{16}$$

is the partition function, is calculated using, for example, the QMC algorithm discussed in Sec. 2.2 and used to determine the cluster self-energy

$$\Sigma_c(\boldsymbol{K}, i\omega_n) = \mathcal{G}_0^{-1}(\boldsymbol{K}, i\omega_n) - G_c^{-1}(\boldsymbol{K}, i\omega_n)\,. \tag{17}$$

Then, using this new result for $\Sigma_c(\boldsymbol{K}, i\omega_n)$ in Eq. (12), steps (11) to (17) are iterated to self-consistency, i.e., until $\Sigma_c(\boldsymbol{K}, i\omega_n)$ does not change anymore between iterations. A sketch of the self-consistency loop to obtain the DCA self-energy $\Sigma^{DCA}(\boldsymbol{k})$ is given in Fig. 2, and Fig. 3 shows a typical result taken from Ref. [5] for a Hubbard model with $t' = -0.15\,t$ and $U = 7\,t$ at a filling $\langle n \rangle = 0.95$ and temperature $T = 0.33\,t$, which has been obtained with the quantum Monte Carlo cluster solver described in Sec. 2.2. Here, the imaginary part of $\Sigma^{DCA}(\boldsymbol{k}, \pi T)$ is plotted for the first Matsubara frequency versus $\boldsymbol{k}$ along a high-symmetry path in the Brillouin zone. For this case, the self-energy has a pronounced momentum dependence and one sees the basic approximation of the DCA: The self-energy is constant within a $\boldsymbol{K}$-patch and has a

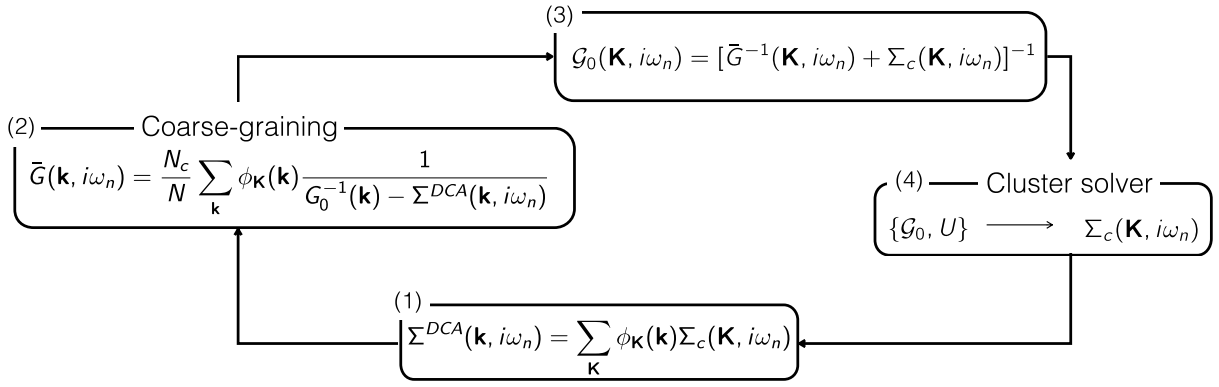

Fig. 2: The DCA self-consistency loop: (1) *To initialize the algorithm, one starts with a cluster self-energy $\Sigma_c(\boldsymbol{K}, i\omega_n)$, which is usually taken from a previous calculation, for example at a higher temperature, or set to zero. From $\Sigma_c(\boldsymbol{K}, i\omega_n)$, the lattice self-energy $\Sigma^{DCA}(\boldsymbol{k}, i\omega_n)$ is constructed using a piecewise-constant continuation of $\Sigma_c(\boldsymbol{K}, i\omega_n)$.* **(2)** *$\Sigma^{DCA}(\boldsymbol{k}, i\omega_n)$ is then used in the coarse-graining of the Green's function to give $\bar{G}(\boldsymbol{K}, i\omega_n)$.* **(3)** *From $\bar{G}(\boldsymbol{K}, i\omega_n)$, one then calculates the corresponding bare Green's function of the cluster, $\mathcal{G}_0(\boldsymbol{K}, i\omega_n)$, by removing the cluster self-energy $\Sigma_c(\boldsymbol{K}, i\omega_n)$.* **(4)** *The bare cluster Green's function $\mathcal{G}_0(\boldsymbol{K}, i\omega_n)$ is used together with the interaction U to set up the effective cluster model, which is solved with a cluster solver such as the QMC algorithm discussed in Sec. 2.2. This provides a new result for the cluster self-energy $\Sigma_c(\boldsymbol{K}, i\omega_n)$, which is used in the next iteration in step (1).*

step discontinuity at the boundary between the patches. In addition, it is apparent that different clusters can give large differences in $\Sigma^{DCA}(\boldsymbol{k})$. This is especially clear in the case of the 16A and 16B clusters (see Fig. 1), which have the same size but different locations and shapes of the coarse-graining patches. In principle, these finite-size effects can be mitigated by carrying out calculations for larger clusters. In some cases, calculations for very large clusters are possible and one can perform finite size scaling to obtain the exact infinite cluster size result. Usually, however, the increase in numerical complexity associated with going to larger clusters limits calculations to relatively small clusters for which this problem persists.

2.2 Quantum Monte Carlo cluster solver

The DCA algorithm requires the calculation of the Green's function and the self-energy of the effective cluster problem as defined by the action in Eq. (14). While the determinantal QMC (DQMC) technique [8] is the method of choice for unbiased calculations of 2D finite-size lattices, here one deals with a finite-size cluster embedded in a dynamic mean field, and other methods that can treat this coupling to a fermionic bath are necessary. The Hirsch-Fye QMC algorithm was originally developed to study the properties of magnetic impurities hybridized with conduction electrons in metals [10] and later extended to solve the effective cluster problem in the DCA [11]. Just like the DQMC algorithm, this method uses a Suzuki-Trotter decomposition of the partition function and therefore has time discretization errors. In recent years, however,

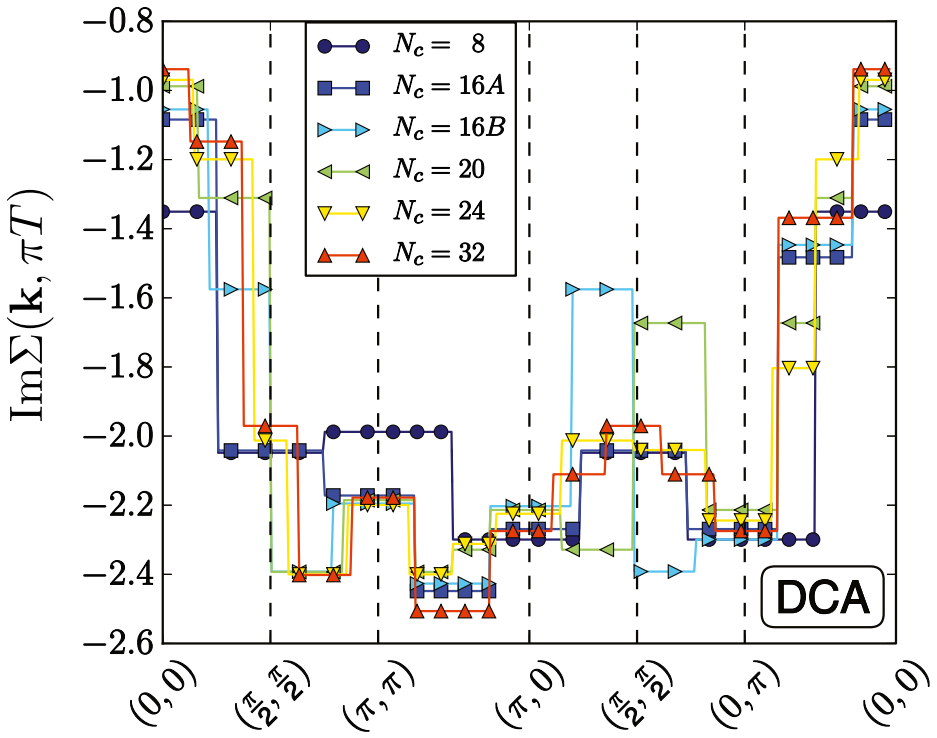

Fig. 3: DCA self-energy: *DCA results for the imaginary part of the lattice self-energy* $\Sigma(\boldsymbol{k}, \pi T)$ *for a Hubbard model with* $U = 7\,t$, $t' = -0.15t$, $\langle n \rangle = 0.95$ *at a temperature* $T = 0.33\,t$. *The DCA approximation gives a self-energy with jump discontinuities between the coarse-graining patches and which depends strongly on the location and shape of the patches (*$N_c = 16A$ *vs. 16B).*

a number of continuous-time QMC (CT-QMC) methods have been developed [12], which are free from time discretization errors and which are more efficient than the Hirsch-Fye algorithm. Of these, we will discuss the continuous-time auxiliary-field (CT-AUX) QMC algorithm [13], which has been developed specifically for the type of large cluster DCA calculations we are interested in.

The CT-AUX algorithm is formally similar to the Hirsch-Fye QMC algorithm in that it employs an auxiliary-field decoupling of the interaction term, H_{int} in Eq. (2). But instead of the time discretization, it performs a weak-coupling expansion of the interaction term. Monte Carlo sampling is then performed in the combined space of perturbation expansion order and time-ordered configurations for a given order. The method yields numerically exact results that are continuous in time since the positions along the imaginary time axis are variable and not fixed as in Hirsch-Fye. In the following, we sketch the basic idea of this approach and refer the reader to Refs. [12, 13] for a detailed discussion.

One starts by expanding the partition function, Eq. (16), in powers of H_{int} to which an arbitrary constant term $-K/\beta$ with non-zero K has been added. Then, one applies the auxiliary-field decomposition [14]

$$1 - \frac{\beta U}{K} \sum_i \left[n_{i\uparrow} n_{i\downarrow} - \frac{1}{2}(n_{i\uparrow} + n_{i\downarrow}) \right] = \frac{1}{2N_c} \sum_{i, s_i = \pm 1} e^{\gamma s_i (n_{i\uparrow} - n_{i\downarrow})} , \tag{18}$$

Fig. 4: Configuration in the CT-AUX QMC algorithm: *The CT-AUX QMC algorithm samples different expansion orders in an interaction expansion and time-ordered configurations of vertices with cluster site x, imaginary time τ, and auxiliary Ising spin s for a given expansion order k. Here we show a representation of an order $k = 3$ configuration* $((x_1, \tau_1, s_1), (x_2, \tau_2, s_2), (x_3, \tau_3, s_3))$.

with $\cosh(\gamma) = 1 + U\beta N_c/2K$. With this, the partition function

$$Z = \sum_{k=0}^{\infty} \sum_{s_1 \dots s_k = \pm 1} \int_0^\beta d\tau_1 \dots \int_{\tau_{k-1}}^\beta d\tau_k \left(\frac{K}{2\beta N_c}\right)^k Z_k(\{x, \tau, s\}_k) \tag{19}$$

then becomes a sum over expansion orders k and auxiliary-spin configurations $s_1 \dots s_k$ of terms

$$Z_k(\{x, \tau, s\}_k) = Z_0 \prod_\sigma \det N_\sigma^{-1}(\{x, \tau, s\}_k)\,. \tag{20}$$

Here, $\{x, \tau, s\}_k$ is a configuration of k vertices with cluster site x, imaginary time τ and auxiliary spin s (see Fig. 4) and $\boldsymbol{N}_\sigma$ is a $k \times k$ matrix

$$[N_\sigma^{-1}]_{ij} = [e^{\gamma(-1)^\sigma s_i}]\,\delta_{ij} - \mathcal{G}_{0,\sigma}(x_i, \tau_i; x_j, \tau_j)\,. \tag{21}$$

This equation expresses the weight of a configuration $\{x, \tau, s\}_k$ for expansion order k in terms of the bare cluster Green's function $\mathcal{G}_{0,\sigma}(x_i, \tau_i; x_j, \tau_j)$, the interaction U (through γ), and the product of determinants of two matrices $\boldsymbol{N}_\sigma$.

The Monte Carlo algorithm then samples the partition function by randomly creating and removing auxiliary spins s at different times τ and locations x and updating the $\boldsymbol{N}_\sigma$ matrices using fast update formulas [13]. In the case of a single-spin update, this takes the form of a rank-1 update (vector outer product). In order to improve the efficiency of the algorithm, k_s subsequent rank-1 updates can be rewritten as a rank-k_s update [15]. Measurements of the single-particle and two-particle Green's functions are made in a similar manner as in the Hirsch-Fye algorithm. That is, after the auxiliary field has been introduced, one has a Wick's theorem for decomposing products of time-ordered operators. To avoid time-discretization problems and for improved efficiency, it is beneficial to Fourier-transform to frequency and momentum space before carrying out the measurements [12]. Due to the random times of the vertices, non-equidistant fast Fourier transform algorithms are employed to further improve efficiency [16].

2.3 Comparison with finite-size calculations

Both types of calculations, finite-size and DCA, make the assumption that correlations are short-ranged and contained within a finite-size cluster. In contrast to studies of finite-size systems,

however, in which the exact state of a cluster with N_c sites is determined and regarded as an approximation to the bulk thermodynamic limit, the DCA, for a given cluster size N_c, gives approximate results for the thermodynamic limit. Both methods give the exact result as $N_c \to \infty$, but only the DCA has a non-trivial limit as $N_c \to 1$. For $N_c = 1$, the single DCA patch extends over the full Brillouin zone (see Fig. 1), the coarse-grained Green's function in Eq. (11) becomes the local Green's function, and the equations of the Dynamical Mean-Field Approximation [17] are recovered.

The difference between a finite-size and a DCA calculation becomes clear when writing the bare cluster Green's function $\mathcal{G}_0(\boldsymbol{K}, i\omega_n)$ that enters the bilinear part of the effective action given in Eq. (14) as [1]

$$\mathcal{G}_0(\boldsymbol{K}, i\omega_n) = \frac{1}{i\omega_n + \mu - \bar{\varepsilon}_{\boldsymbol{K}} - \Gamma(\boldsymbol{K}, i\omega_n)} \,. \tag{22}$$

Here, $\bar{\varepsilon}_{\boldsymbol{K}} = N_c/N \sum_{\boldsymbol{k}} \phi_{\boldsymbol{K}}(\boldsymbol{k})\, \varepsilon_{\boldsymbol{k}}$ is the coarse-grained average of the dispersion, and the hybridization function

$$\Gamma(\boldsymbol{K}, i\omega_n) = \frac{\frac{N_c}{N} \sum_{\boldsymbol{k}} \phi_{\boldsymbol{K}}(\boldsymbol{k})\, \delta t^2_{\boldsymbol{K}}(\boldsymbol{k})\, G(\boldsymbol{k}, i\omega_n)}{1 + \frac{N_c}{N} \sum_{\boldsymbol{k}} \phi_{\boldsymbol{K}}(\boldsymbol{k})\, \delta t_{\boldsymbol{K}}(\boldsymbol{k})\, G(\boldsymbol{k}, i\omega_n)} \tag{23}$$

with $\delta t_{\boldsymbol{K}}(\boldsymbol{k}) = \varepsilon_{\boldsymbol{k}} - \bar{\varepsilon}_{\boldsymbol{K}}$ describes the coupling of the cluster degrees of freedom to the remaining sites of the bulk lattice in an averaged, mean-field manner. This is in contrast to the finite-size case, in which one uses the bare Green's function of an isolated cluster, i.e. $G_0(\boldsymbol{K}, i\omega_n) = [i\omega_n + \mu - \varepsilon_{\boldsymbol{K}}]^{-1}$, in the action. For the DCA, $\mathcal{G}_0$ in Eq. (22) has the form of a Green's function of a non-interacting cluster with momenta $\boldsymbol{K}$, where each $\boldsymbol{K}$ is coupled to a dynamic mean field given by $\Gamma(\boldsymbol{K}, i\omega_n)$. As one sees from Eq. (23), $\Gamma(\boldsymbol{K}, i\omega_n)$ describes the effects of the $\boldsymbol{k}$ momenta surrounding $\boldsymbol{K}$ in an averaged fashion. As a consequence, for a given finite cluster, the DCA gives results that are usually closer to the thermodynamic limit than a finite-size calculation [11, 18].

Sign problem

The most significant challenge of QMC calculations of fermionic systems is the so-called fermion sign problem [19]. In the general case of a Hubbard model at finite doping, it arises from a negative product of determinants in the weight Z_k (Eq. (20)) of a configuration that is used to calculate the probability of accepting an update in the Monte Carlo procedure. For a simple Hubbard model, it leads to a statistical error that grows exponentially in the number of cluster sites N_c, the inverse temperature β, and the size of the Coulomb repulsion U. Just like finite-size QMC calculations, this sign problem is also encountered in DCA and DCA$^+$ calculations when a QMC algorithm such as the CT-AUX algorithm described in Sec. 2.2 is used to solve the effective cluster problem.

DCA QMC calculations were shown to have a much less severe sign problem than finite-size QMC calculations (see Fig. 5). Lacking a rigorous mathematical justification, this was attributed to the action of the mean-field host on the cluster [11]. In any case, this significant reduction of the severity of the sign problem in the DCA has enabled access to much lower temperatures than those that can be reached in finite-size systems.

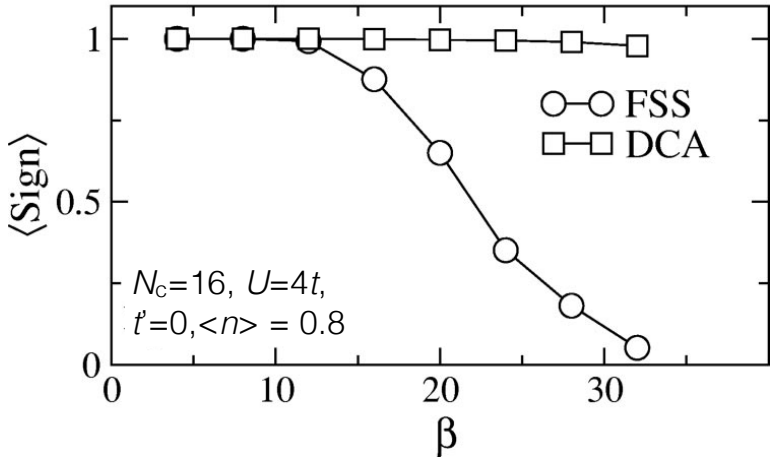

Fig. 5: DCA reduction of the sign problem: *The average QMC sign compared between finite-size calculation (FSS) and DCA for a 16-site cluster with $U = 4t$ and $\langle n \rangle = 0.8$. The DCA algorithm reduces the sign problem of finite-size QMC significantly. Figure taken from Ref. [11].*

2.4 Calculation of response functions

Response functions, such as the magnetic susceptibility, provide information on the response of a system to an external field, as well as on the nature of the dominant fluctuations and possible instabilities of the system towards spontaneous symmetry breaking. The calculations of these functions requires extensions to the single-particle formalism described in the previous sections. They either require an explicit calculation on the single-particle level in the presence of a symmetry-breaking field or a calculation of two-particle Green's functions, from which the susceptibilities can be calculated [1]. Here we discuss the second approach and refer the reader to Ref. [1] for the first approach.

General formalism

As an illustrative example, let us consider the "pair-field" susceptibility

$$P_\varphi(T) = \int_0^\beta d\tau \, \langle \Delta_\varphi(\tau) \Delta_\varphi^\dagger(0) \rangle \tag{24}$$

which gives the superconducting response of a system to an external "pair-field" that couples to the pairing operator

$$\Delta_\varphi^\dagger = \frac{1}{\sqrt{N}} \sum_{\boldsymbol{k}} g_\varphi(\boldsymbol{k}) \, c_{\boldsymbol{k}\uparrow}^\dagger c_{-\boldsymbol{k}\downarrow}^\dagger \, . \tag{25}$$

Here, $g_\varphi(\boldsymbol{k})$ is a form factor that describes the momentum-dependence and symmetry of the pair wavefunction. For a pair with internal $d_{x^2-y^2}$-wave symmetry, for example, a state that is relevant to the copper-oxide high-temperature superconductors as well as to the 2D Hubbard model, one has

$$g_{d_{x^2-y^2}}(\boldsymbol{k}) = \cos k_x - \cos k_y \tag{26}$$

where $\boldsymbol{k} = (k_x, k_y)$. This arranges the electrons of the corresponding real-space pair on nearest-neighbor sites with a $d_{x^2-y^2}$ phase ($+1$ along $\pm x$ and -1 along $\pm y$). For a conventional s-wave pair, on the other hand, one simply has $g_s(\boldsymbol{k}) = 1$.
The pair-field susceptibility $P_\varphi(T)$ may be calculated from the two-particle Green's function

$$G_{2,\sigma_1\ldots\sigma_4}(x_1, x_2; x_3, x_4) = -\langle T_\tau \, c_{\sigma_1}(x_1) c_{\sigma_2}(x_2) c^\dagger_{\sigma_3}(x_3) c^\dagger_{\sigma_4}(x_4) \rangle \, . \tag{27}$$

Fourier-transforming on both the space and time variables gives $G_{2\sigma_1\ldots\sigma_4}(k_4, k_3; k_2, k_1)$ with $k = (\boldsymbol{k}, i\omega_n)$. With this, one has

$$P_\varphi(T) = \frac{T^2}{N^2} \sum_{k,k'} g_\varphi(\boldsymbol{k}) \, G_{2,\uparrow\downarrow\downarrow\uparrow}(k, -k, -k', k') \, g_\varphi(\boldsymbol{k}') \tag{28}$$

The way G_2 is calculated in the DCA algorithm is similar to the way G is calculated at the single-particle level. Just as the Dyson equation (8) relates the Green's function to the self-energy, the Bethe-Salpeter equation (BSE) relates G_2 to the irreducible vertex function $\Gamma_\alpha(k_1, k_2; k_3, k_4)$ for channel α.[1] For example, for the particle-particle channel, which is relevant here, one has

$$\begin{aligned} G_2(k, q-k, q-k', k') &= G_\uparrow(k) \, G_\downarrow(q-k) \, \delta_{k,k'} \\ &- \frac{T}{N} \sum_{k''} G_\uparrow(k) \, G_\downarrow(q-k) \, \Gamma_{pp}(k, q-k, q-k'', k'') \, G_2(k'', q-k'', q-k', k') \, . \end{aligned} \tag{29}$$

Here we have used momentum, energy and spin conservation to reduce the dependence on four variables $k_1 \ldots k_4$ to three variables k, k', and q, where $q = (\boldsymbol{q}, i\omega_m)$ is the combined transferred momentum and bosonic frequency ω_m. A similar expression is obtained in the particle-hole channels. Furthermore, because of the spin-rotational invariance of the Hubbard model, it is convenient to separate the particle-particle channel into singlet and triplet parts and the particle-hole channel into a magnetic part, which carries spin $S = 1$, and a charge density part, which has $S = 0$.

Approximation of the irreducible vertex

Just like the DCA self-energy $\Sigma(\boldsymbol{k})$ is approximated by the cluster self-energy $\Sigma_c(\boldsymbol{K})$, the DCA irreducible vertex function is approximated by a piecewise constant continuation of the corresponding cluster irreducible vertex function [11]

$$\Gamma_\alpha(k, k') = \sum_{\boldsymbol{K}, \boldsymbol{K}'} \phi_{\boldsymbol{K}}(\boldsymbol{k}) \, \Gamma_{c,\alpha}(K, K') \, \phi_{\boldsymbol{K}'}(\boldsymbol{k}') \, . \tag{30}$$

Here, for simplicity, we have used an abbreviated notation and included the transferred momentum q in the "channel" α, so that, for example, $\Gamma_{pp,q}(k, k') \equiv \Gamma_{pp}(k, q-k, q-k', k')$ in the

[1] Depending on how particles and holes are involved in the scattering, one can define particle-particle and particle-hole channels

particle-particle channel. Like the self-energy, the cluster-irreducible vertex $\Gamma_{c,\alpha}(k,k')$ is determined from the solution of the cluster problem, that is by calculating the cluster two-particle correlation function $G_{2,c,\alpha}(k,k')$ and extracting $\Gamma_{\alpha,c}(k,k')$ from the BSE on the cluster [11]. For example, in the particle-particle channel for $Q=0$

$$G_{2,c}(K,K') = G_{c,\uparrow}(K)\,G_{c,\downarrow}(-K)\delta_{K,K'} - \frac{T}{N}\sum_{K''} G_{c,\uparrow}(K)\,G_{c,\downarrow}(-K)\Gamma_{c,pp}(K,K'')\,G_{2,c}(K'',K') \tag{31}$$

Writing this in matrix notation in K,K', one then has

$$\boldsymbol{\Gamma}_{c,pp} = -\frac{N}{T}\left[[\boldsymbol{G}^0_{2,c}]^{-1} - [\boldsymbol{G}_{2,c}]^{-1}\right], \tag{32}$$

where $G^0_{2,c}(K,K') = G_{c,\uparrow}(K)\,G_{c,\downarrow}(-K)\,\delta_{K,K'}$. The approximation in Eq. (30) is then used in the lattice BSE in Eq. (29) to calculate the two-particle Green's function on the lattice and from it the response function. Since $\Gamma_{c,\alpha}(K,K')$ depends on the cluster momenta $\boldsymbol{K}$ only, the problem may be further simplified by coarse-graining over momenta $\boldsymbol{k}$ within a patch around $\boldsymbol{K}$ for cases where the form factor $g_\varphi = 1$. For cases with a momentum- dependent form-factor $g_\varphi(\boldsymbol{k})$, a slightly modified version of this procedure is necessary [11].

Bethe-Salpeter eigenvalues and eigenfunctions

An alternative approach to determining the nature of the low-energy fluctuations is based on calculating the eigenvalues and eigenvectors of the BSE kernel [20–22]. For example, in the particle-particle channel with $q=0$, one solves the eigenvalue equation

$$-\frac{T}{N}\sum_{k'}\Gamma_{pp}(k,k')\,G_{\uparrow}(k')\,G_{\downarrow}(-k')\,g_\alpha(k') = \lambda_\alpha\,g_\alpha(k)\,, \tag{33}$$

with similar equations for the particle-hole channels. Note that it is possible to reconstruct the two-particle Green's function from these eigenvalues and eigenvectors

$$G_{2,pp}(k,k') = \sum_\alpha G_{\uparrow}(k)\,G_{\downarrow}(-k)\,\frac{g_\alpha(k)\,g^*_\alpha(k')}{1-\lambda_\alpha}\,. \tag{34}$$

From this it becomes clear that an instability occurs when the leading eigenvalue λ_α becomes 1, and the momentum and frequency structure of the interaction is then reflected in the structure of the corresponding eigenvector $g_\alpha(k)$. This approach is in many ways more powerful than calculating the response function directly, because here one does not have to assume a given form factor $g_\alpha(\boldsymbol{k})$ and therefore cannot "miss" the structure of the dominant correlations.
Using the DCA (30) for the lattice vertex $\Gamma_{pp}(k,k')$ and assuming that the eigenvectors (as irreducible quantities) only depend on the cluster momenta $\boldsymbol{K}$, one can then sum (coarse-grain) over the Green's function legs to obtain an equation that only depends on coarse-grained and cluster quantities [21, 22]

$$-\frac{T}{N_c}\sum_{K'}\Gamma_{c,pp}(K,K')\,\chi_{0,pp}(K')\,g_\alpha(K') = \lambda_\alpha\,g_\alpha(K)\,, \tag{35}$$

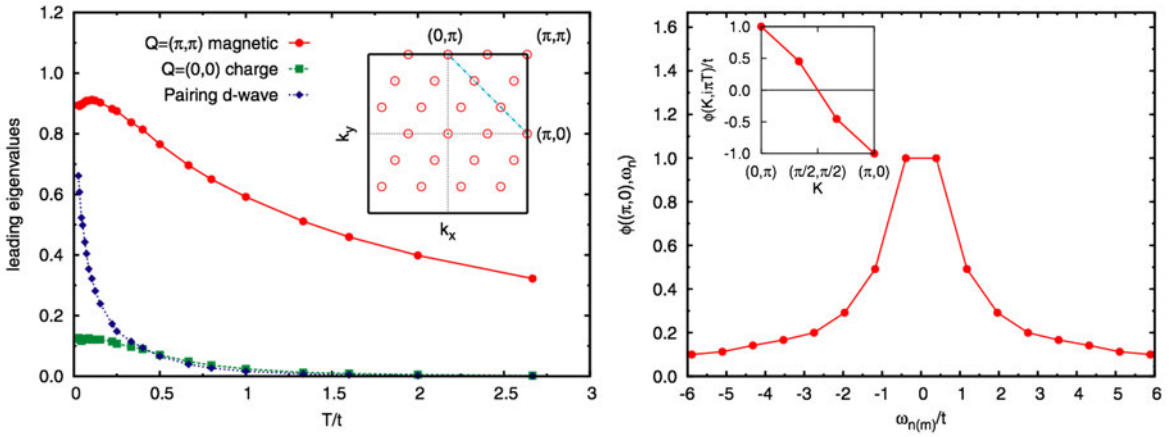

Fig. 6: Example of the solution of the Bethe-Salpeter equation in the various two-particle channels for a Hubbard model with $\mathrm{U} = 4\mathrm{t}$ and $\langle \mathrm{n} \rangle = 0.85$: *Left panel: The leading eigenvalue in the* $\mathbf{Q} = (\pi, \pi)$, $\omega_m = 0$ *particle-hole magnetic channel dominates but saturates at low temperatures. The leading eigenvalue in the singlet* $\mathbf{Q} = 0$, $\omega_m = 0$ *particle-particle channel is found to have* $d_{x^2-y^2}$ *symmetry and increases towards 1 at low temperatures. The largest eigenvalue in the charge density particle-hole channel remains small. Right panel: The momentum dependence of the leading eigenvector* $\phi_d(\boldsymbol{K}, \pi T)$ *in the singlet particle-particle channel shows its* $d_{x^2-y^2}$ *dependence. Its frequency dependence reflects the frequency dependence of the pairing interaction* Γ_{pp}*. Figures taken from Ref. [21].*

with $\chi_{0,pp}(K) = N_c/N \sum_{\boldsymbol{k}} \phi_{\boldsymbol{K}}(\boldsymbol{k})\, G_\uparrow(k)\, G_\downarrow(-k)$. While this reduces the complexity significantly, it also lowers the momentum resolution to the discrete set of cluster momenta $\boldsymbol{K}$. An example of the resulting leading eigenvalues and eigenvectors in the singlet particle-particle and also particle-hole magnetic and charge channels is shown in Fig. 6. These results illustrate how the calculation and analysis of the eigenvalues and eigenvectors of the BSE kernel provides a useful, unbiased method for determining the nature of the leading correlations of interacting many-body systems.

3 The DCA$^+$ method

The DCA$^+$ algorithm was developed as an extension of the DCA in order to introduce a lattice self-energy with continuous momentum $\boldsymbol{k}$ dependence and thus reduce its cluster-shape and size dependence [5]. Formally, this is achieved by expanding the lattice self-energy $\Sigma(\boldsymbol{k})$ into an arbitrarily large set of basis functions, instead of the patch functions that are used in the expansion of the DCA self-energy in Eq. (12). This means that in contrast to the DCA, where the lattice self-energy $\Sigma(\boldsymbol{k})$ is given by the cluster self-energy $\Sigma_c(\boldsymbol{K})$, in the DCA$^+$ they are generally different.

3.1 General formalism

Using the identity

$$\frac{N_c}{N} \sum_{\boldsymbol{k}} \phi_{\boldsymbol{K}}(\boldsymbol{k})\, \phi_{\boldsymbol{K}'}(\boldsymbol{k}) = \delta_{\boldsymbol{K}\boldsymbol{K}'}\,, \tag{36}$$

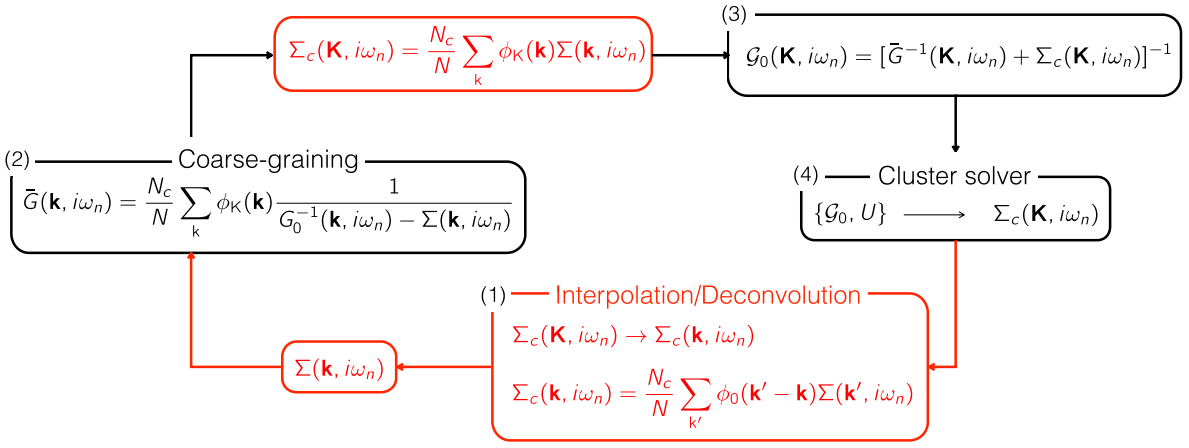

Fig. 7: DCA$^+$ self-consistency loop: *Parts colored in black are shared with the DCA algorithm, parts colored in red are additional steps.* **(1)** *To initialize the algorithm, one starts with a cluster self-energy $\Sigma_c(\boldsymbol{K}, i\omega_n)$. This is usually taken from a previous calculation, for example at a higher temperature, or set to zero. From $\Sigma_c(\boldsymbol{K}, i\omega_n)$, the lattice self-energy $\Sigma(\boldsymbol{k}, i\omega_n)$ is constructed using an interpolation of $\Sigma_c(\boldsymbol{K})$ followed by a deconvolution. Here, the interpolated cluster self-energy is also symmetrized according to the point-group symmetries of the lattice.* **(2)** *$\Sigma(\boldsymbol{k}, i\omega_n)$ is then used in the coarse-graining of the Green's function to give $\bar{G}(\boldsymbol{K}, i\omega_n)$.* **(3)** *From $\bar{G}(\boldsymbol{K}, i\omega_n)$, one then calculates the corresponding bare Green's function of the cluster, $\mathcal{G}_0(\boldsymbol{K}, i\omega_n)$, by removing the cluster self-energy $\Sigma_c(\boldsymbol{K}, i\omega_n)$. This cluster/coarse-grained self-energy is obtained by coarse-graining the lattice self-energy $\Sigma(\boldsymbol{k}, i\omega_n)$. It is equal to the cluster self-energy that was used in the interpolation/deconvolution step unless it did not converge.* **(4)** *The bare cluster Green's function $\mathcal{G}_0(\boldsymbol{K}, i\omega_n)$ is used together with the interaction U to set up the effective cluster model, which is solved with a cluster solver such as the QMC algorithm discussed in Sec. 2.2. This provides a new result for the cluster self-energy $\Sigma_c(\boldsymbol{K}, i\omega_n)$, which is used in the next iteration in step (1).*

for the patch functions defined in Eq. (9), one reverses the relation in Eq. (12) to a coarse-graining relation for the self-energy

$$\Sigma_c(\boldsymbol{K}) = \frac{N_c}{N} \sum_{\boldsymbol{k}} \phi_{\boldsymbol{K}}(\boldsymbol{k})\, \Sigma(\boldsymbol{k})\,. \tag{37}$$

This relation forms the basic equation of the DCA$^+$ algorithm. It is fundamentally different from the DCA equation (12) in that it allows the lattice self-energy $\Sigma(\boldsymbol{k})$ to have continuous momentum dependence. Eq. (37) is trivially satisfied by the DCA approximation to $\Sigma(\boldsymbol{k})$ in Eq. (12). In general, however, Eq. (37) allows for a more physical approximation in which the lattice self-energy $\Sigma(\boldsymbol{k})$ can retain a smooth and continuous $\boldsymbol{k}$ dependence without the step discontinuities of the standard DCA. The inversion of Eq. (37) and extraction of a lattice self-energy $\Sigma(\boldsymbol{k})$ is a challenging task, which in Ref. [5] is solved by an initial interpolation of the cluster self-energy $\Sigma_c(\boldsymbol{K})$ and a subsequent deconvolution of a generalization of Eq. (37). This approach is described in Sec. 3.2. Assuming that this equation can be inverted to find the lattice

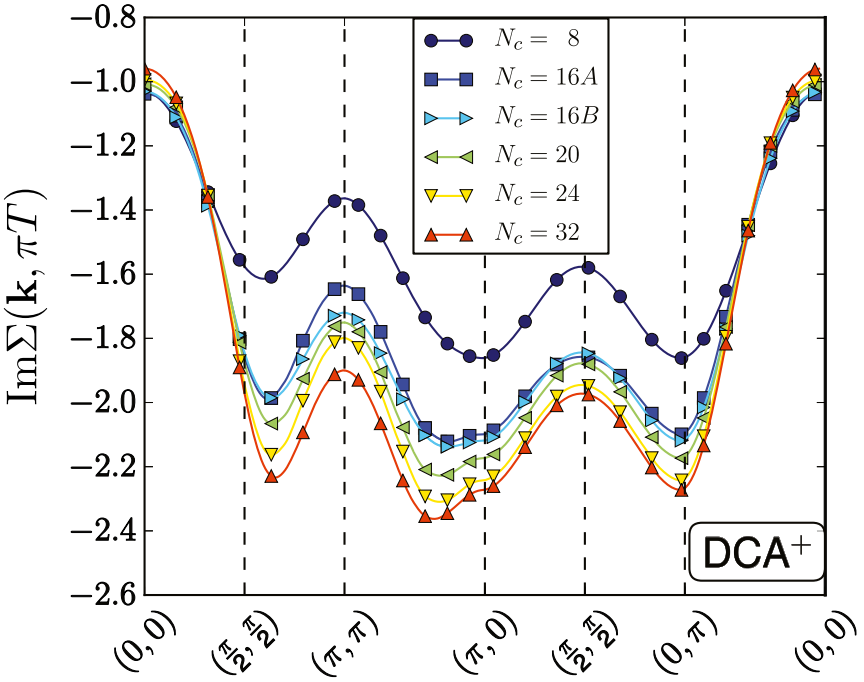

Fig. 8: DCA$^+$ self-energy: *DCA$^+$ results for the imaginary part of the lattice self-energy $\Sigma(\boldsymbol{k}, \pi T)$ for a Hubbard model with the same parameters as those that were used in the plot of the DCA self-energy in Fig. 3, i.e., $U = 7\,t$, $t' = -0.15\,t$, $\langle n \rangle = 0.95$ and $T = 0.33\,t$. Compared with the DCA self-energy in Fig. 3, the DCA$^+$ approximation gives a smooth momentum dependence with much weaker cluster shape and size dependence. Figure taken from Ref. [5].*

self-energy $\boldsymbol{\Sigma}(\boldsymbol{k})$, one then proceeds by calculating the coarse-grained Green's function

$$\bar{G}(\boldsymbol{K}, i\omega_n) = \frac{N_c}{N} \sum_{\boldsymbol{k}} \phi_{\boldsymbol{K}}(\boldsymbol{k}) \, \frac{1}{G_0^{-1}(\boldsymbol{k}) - \Sigma(\boldsymbol{k}, i\omega_n)} \,. \tag{38}$$

just as in the standard DCA algorithm. Note, however, that in contrast to the DCA, here the full lattice self-energy with continuous momentum $\boldsymbol{k}$ dependence enters in the coarse-graining of the Green's function. The remainder of the algorithm remains identical to the DCA algorithm, including in particular the structure of the effective cluster problem. A detailed description of the self-consistent loop of the DCA$^+$ is given in Fig. 7.

Results for the lattice self-energy $\Sigma(\boldsymbol{k})$ obtained in the DCA$^+$ algorithm are shown in Fig. 8 for a Hubbard model with $t' = -0.15\,t$ and $U = 7\,t$ at a filling $\langle n \rangle = 0.95$. Here, the imaginary part of the lattice self-energy $\Sigma(\boldsymbol{k}, \pi T)$ at the first Matsubara frequency is shown for various cluster sizes. Compared to the corresponding DCA results in Fig. 3, the DCA$^+$ algorithm by construction gives a smooth and therefore much more physical momentum dependence. One clearly sees that it gives a much more systematic convergence by reducing the cluster shape and size dependence of the DCA. This is especially clear for the 16A and 16B clusters. While the DCA self-energies in Fig. 3 differ significantly between these two clusters, the DCA$^+$ results are almost identical with the exception of a small region around (π, π). One should also stress that in the DCA$^+$, the full lattice point-group symmetries are restored in the interpolation/deconvolution step for clusters that are not fully symmetric, while this is not the case in the DCA. This can be seen, for example, in the case of the 16B cluster.

3.2 Determination of lattice quantities from cluster quantities

The non-trivial task in the DCA$^+$ algorithm is the generation of a lattice self-energy $\Sigma(\boldsymbol{k})$ with continuous momentum $\boldsymbol{k}$ dependence that satisfies the coarse-graining relation in Eq. (37) [5]. This inversion problem is obviously underdetermined since there are more $\boldsymbol{k}$ points than cluster $\boldsymbol{K}$ points. One can imagine interpolating the cluster self-energy $\Sigma_c(\boldsymbol{K})$ onto the fine $\boldsymbol{k}$ grid to give $\Sigma_c(\boldsymbol{k})$. This is discussed in more detail below. Then, it is convenient to generalize the coarse-graining relation in Eq. (37) to a convolution

$$\Sigma_c(\boldsymbol{k}) = \frac{N_c}{N} \sum_{\boldsymbol{k}'} \phi_0(\boldsymbol{k}' - \boldsymbol{k}) \Sigma(\boldsymbol{k}') \,. \tag{39}$$

Here, we have used the fact that one can write $\phi_{\boldsymbol{K}}(\boldsymbol{k}') = \phi_{\boldsymbol{K}=0}(\boldsymbol{k}' - \boldsymbol{K})$ and then generalized the cluster momentum $\boldsymbol{K}$ to $\boldsymbol{k}$ to give $\phi_0(\boldsymbol{k}' - \boldsymbol{k})$. Eq. (39) now has the form of a convolution, which needs to be inverted. One could, for example, imagine expanding the lattice self-energy in terms of cubic Hermite splines for fixed frequency $i\omega_n$ [5]

$$\Sigma(\boldsymbol{k}) = \sum_i \mathcal{B}_{i\omega_n}(\boldsymbol{k} - \boldsymbol{k}_i) \sigma(\boldsymbol{k}_i), \tag{40}$$

where $\sigma(\boldsymbol{k}_i)$ are the expansion coefficients. Using this expansion, Eq. (39) then becomes

$$\Sigma_c(\boldsymbol{k}_i) = \sum_j P_{ij}\, \sigma(\boldsymbol{k}_j) \tag{41}$$

with the projection matrix

$$P_{ij} = \frac{N_c}{N} \sum_{\boldsymbol{k}} \phi_0(\boldsymbol{k} - \boldsymbol{k}_i)\, \mathcal{B}_{i\omega_n}(\boldsymbol{k} - \boldsymbol{k}_j) \tag{42}$$

and the problem of deconvoluting Eq. (39) has now become a problem of inverting the projection matrix P. The properties of this matrix were discussed in detail in Ref. [5]. There it was shown that P is a near-singular matrix with eigenvalues that become smaller the more the corresponding eigenvector is delocalized. An inversion of P is therefore only possible if eigenvalues smaller than some cut-off ϵ and their corresponding eigenvectors are neglected. If the cluster self-energy is long-ranged and extends beyond the boundary of the real-space cluster, it cannot be represented by the retained smaller-range eigenvectors and eigenvalues of P and the DCA$^+$ calculation does not converge. In this case the cluster size has to be increased. The analysis of the projection matrix and the convergence of a DCA$^+$ calculation thus provides a useful measure of whether the cluster is large enough to capture the correlations.

3.2.1 Determination of lattice self-energy

In practice, the inversion of the projection operator P is numerically unstable, and it is therefore favorable to extract the lattice self-energy $\Sigma(\boldsymbol{k})$ by deconvoluting the interpolated cluster self-energy $\Sigma_c(\boldsymbol{k})$. To this end, a Bayesian based Richardson-Lucy algorithm is used after the cluster self-energy has been interpolated [5].

Interpolation of cluster self-energy

Instead of interpolating $\Sigma_c(\boldsymbol{K})$ directly, it was shown in Ref. [5] that a better result is obtained when $\Sigma_c(\boldsymbol{K})$ is first transformed to $\mathcal{T}(\Sigma_c(\boldsymbol{K}))$ with $\mathcal{T}(z) = (z - i)^{-1}$. This form is similar to the cumulant used in Ref. [23] for the interpolation of cellular dynamical mean-field results. One then applies a Wannier-interpolation [24] to obtain the interpolated cluster self-energy

$$\Sigma_c(\boldsymbol{k}) = \mathcal{T}^{-1}\Big[\sum_{\boldsymbol{R}} e^{-i\boldsymbol{k}\boldsymbol{R}} \underbrace{\Big(\sum_{\boldsymbol{K}} e^{-i\boldsymbol{k}\boldsymbol{R}}\, \mathcal{T}(\Sigma_c(\boldsymbol{K}))\Big)}_{(\mathcal{T}\Sigma)_{\boldsymbol{R}}}\Big]. \tag{43}$$

One should always verify that $(\mathcal{T}\Sigma)_{\boldsymbol{R}}$ does not extend beyond the cluster boundary. When this is the case, this procedure does not introduce any artificial features in the interpolated self-energy, which is often the case with splines, where overshoots are not uncommon. Once the cluster self-energy is interpolated, lattice point-group symmetries are imposed on the interpolated self-energy $\Sigma(\boldsymbol{k})$. This is especially important for clusters that do not have the full lattice symmetry, such as the 16B cluster in Fig. 1. The interpolated cluster self-energy $\Sigma_c(\boldsymbol{k})$ from Eq. (43) is then used in the convolution in Eq. (39) to determine the lattice self-energy $\Sigma(\boldsymbol{k})$.

Deconvolution of lattice self-energy

Since the patch function $\phi_0(\boldsymbol{k})$ in Eq. (39) acts as a box-car filter on $\Sigma(\boldsymbol{k})$, one can apply the Richardson-Lucy algorithm [25, 26] to solve this deconvolution problem. This algorithm is based on Bayesian inference, which finds the most likely solution $\Sigma(\boldsymbol{k})$ by using an iteration procedure [5]

$$\Sigma_{i+1}(\boldsymbol{k}) \leftarrow \Sigma_i(\boldsymbol{k}) \int d\boldsymbol{k}'\, \frac{\phi_0(\boldsymbol{k} - \boldsymbol{k}')\, \Sigma_c(\boldsymbol{k}')}{\int d\boldsymbol{k}''\, \phi_0(\boldsymbol{k}' - \boldsymbol{k}'')\, \Sigma_i(\boldsymbol{k}'')}\,. \tag{44}$$

This procedure is carried out separately for the real and imaginary parts of the self-energy. As discussed in Ref. [5], this algorithm converges well when correlations are short-ranged and contained within the cluster. When the range of the correlations exceeds the cluster, one generally finds that this algorithm converges slowly and gives an estimate for the lattice self-energy $\Sigma(\boldsymbol{k})$ that, after coarse-graining, deviates considerably from the cluster self-energy $\Sigma_c(\boldsymbol{K})$ and thus does not satisfy the DCA$^+$ constraint in Eq. (37). Fig. 9 shows the result of this procedure for a calculation of a 32-site cluster, for which the cluster self-energy does not exceed the cluster size and thus the Richardson-Lucy procedure converges quickly and well. In this case, one sees that the coarse-grained lattice self-energy $\bar{\Sigma}(\boldsymbol{K}) = N_c/N \sum_{\boldsymbol{k}} \phi_{\boldsymbol{K}}(\boldsymbol{k})\, \Sigma(\boldsymbol{k})$ agrees very well with the cluster self-energy $\Sigma_c(\boldsymbol{K})$.

3.2.2 Deconvolution of the irreducible vertex function

In order to extend the DCA$^+$ algorithm to the two-particle level, it is necessary to determine an irreducible vertex function $\Gamma_\alpha(k, k')$ with continuous momentum dependence. Just as for

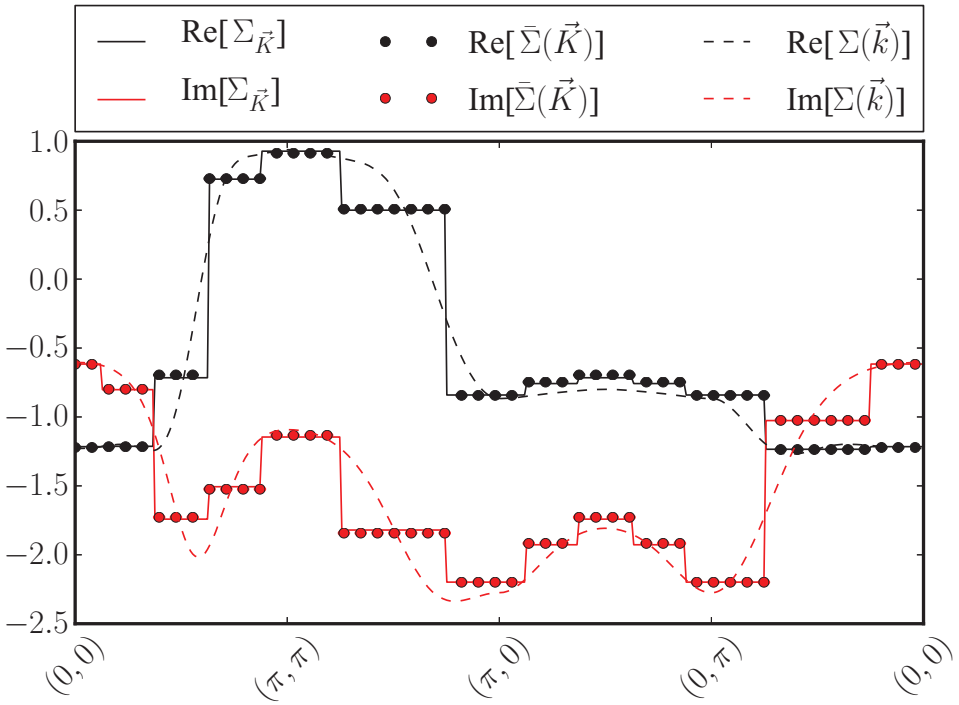

Fig. 9: Richardson-Lucy deconvolution of the lattice self-energy: *DCA$^+$ calculation for a 32-site cluster with $t' = -0.15\,t$ and $U = 7\,t$ at a filling of $\langle n \rangle = 0.95$ and $T = 0.33\,t$. Shown are real (black) and imaginary (red) parts of the continuous lattice self-energy $\Sigma(\boldsymbol{k})$, its coarse-grained result $\bar{\Sigma}(\boldsymbol{K}) = N_c/N \sum_{\boldsymbol{k}} \phi_{\boldsymbol{K}}(\boldsymbol{k})\, \Sigma(\boldsymbol{k})$, and the cluster self-energy $\Sigma_c(\boldsymbol{K})$ for the lowest Matsubara frequency $\omega_0 = \pi T$ for a high-symmetry path in the Brillouin zone. The coarse-grained lattice self-energy $\bar{\Sigma}(\boldsymbol{K})$ agrees very well with the cluster self-energy $\Sigma_c(\boldsymbol{K})$.*

the self-energy, one again uses the identity in Eq. (36), in this case twice, to reverse the DCA relation (30) to get

$$\Gamma_{c,\alpha}(K, K') = \frac{N_c^2}{N^2} \sum_{\boldsymbol{k},\boldsymbol{k}'} \phi_{\boldsymbol{K}}(\boldsymbol{k})\, \Gamma_\alpha(k, k')\, \phi_{\boldsymbol{K}'}(\boldsymbol{k}')\,. \tag{45}$$

In analogy to Eq. (37) for the self-energy, the DCA$^+$ lattice irreducible vertex function is thus related to the cluster irreducible vertex $\Gamma_{c,\alpha}$ through a coarse-graining relation. In the standard DCA algorithm, where $\Gamma_\alpha(k, k')$ is a piecewise-constant continuation (30) of the cluster $\Gamma_{c,\alpha}(K, K')$, this requirement is trivially satisfied. In the DCA$^+$ algorithm, however, one wants to find a $\Gamma_\alpha(k, k')$ with continuous momentum dependence and without step discontinuities that satisfies Eq. (45). Assuming that this equation can be inverted to find the lattice $\Gamma_\alpha(k, k')$, one can then solve the lattice BSE Eq. (29) to calculate the two-particle Green's function G_2, or equivalently, solve the eigenvalue problem (33). Since the full lattice $\boldsymbol{k}$ dependence is retained in the DCA$^+$ formalism, the resulting eigenvectors $g_\alpha(\boldsymbol{k})$ will have smooth momentum dependence.

Evidently, the difficult task is the solution or inversion of the integral equation (45) to obtain the lattice $\Gamma_\alpha(k, k')$. Here, one carries out a similar procedure as for the self-energy by starting

with an interpolation. For this, one uses a singular value decomposition

$$\Gamma_{c,\alpha}(K, K') = \sum_i \sigma_i \, U_i(K) \, V_i(K') \tag{46}$$

to write the cluster vertex in a separable representation. Here, σ_i are the singular values, the columns of U contain the left singular vectors and V contains the right singular vectors. Then, one proceeds by interpolating $U_i(\boldsymbol{K}, i\omega_n)$ and $V_i(\boldsymbol{K}, i\omega_n)$ onto a fine $\boldsymbol{k}$ grid for each $i\omega_n$ to give an interpolated cluster vertex

$$\Gamma_{c,\alpha}(k, k') = \sum_i \sigma_i \, U_i(k) \, V_i(k') \,, \tag{47}$$

where $U_i(k)$ and $V_i(k')$ with $k = (\boldsymbol{k}, i\omega_n)$ are cubic spline interpolations in momentum space of $U_i(K)$ and $V_i(K')$, respectively. In the following we drop the frequency arguments for simplicity. Just as for the self-energy, the coarse-graining in Eq. (45) is then generalized to a convolution

$$\Gamma_{c,\alpha}(k_1, k_2) = \frac{N_c^2}{N^2} \sum_{\boldsymbol{k},\boldsymbol{k}'} \phi_0(\boldsymbol{k} - \boldsymbol{k}_1) \, \Gamma_\alpha(k, k') \, \phi_0(\boldsymbol{k}' - \boldsymbol{k}_2) \,, \tag{48}$$

where again the generalized patch function $\phi_0(\boldsymbol{k} - \boldsymbol{K}) = \phi_{\boldsymbol{K}}(\boldsymbol{k})$. Then, the lattice vertex is expanded into a set of basis functions $\{\mathcal{B}\}$.[2] If cubic Hermite splines [27] are used as basis-functions, the continuous lattice vertex is expanded as

$$\Gamma_\alpha(k, k') = \sum_{i,j} \mathcal{B}_{i\omega_n}(\boldsymbol{k} - \boldsymbol{k}_i) \, \gamma_\alpha(k_i, k_j) \, \mathcal{B}_{i\omega_{n'}}(\boldsymbol{k}' - \boldsymbol{k}_j) \,. \tag{49}$$

Here, the vectors $\boldsymbol{k}_i$ span a fine $\boldsymbol{k}$ grid that covers the first Brillouin zone. Using the expansion in Eq. (49), one can rewrite Eq. (48) as a matrix-equation,

$$\Gamma_{c,\alpha}(k, k') = \sum_{i,j} \Phi_{i\omega_n}(\boldsymbol{k}_1, \boldsymbol{k}_i) \, \gamma^\alpha(k_i, k_j) \, \Phi_{i\omega_{n'}}(\boldsymbol{k}_2, \boldsymbol{k}_j) \tag{50}$$

$$\Phi_{i\omega_n}(\boldsymbol{k}_i, \boldsymbol{k}_j) = \frac{N_c}{N} \sum_{\boldsymbol{k}} \phi_0(\boldsymbol{k} - \boldsymbol{k}_i) \mathcal{B}_{i\omega_n}(\boldsymbol{k} - \boldsymbol{k}_j)$$

Then, using a singular value decomposition of the matrix Φ,

$$\Phi_{i\omega_n}(\boldsymbol{k}_i, \boldsymbol{k}_j) = \sum_i \sigma_i^\Phi \, u_i^\Phi(k_i) \, v_i^\Phi(k_j) \,, \tag{51}$$

(note that all quantities on the right hand side carry an implicit $i\omega_n$-dependence) one can formally invert Eq. (50) and obtain an explicit form for the lattice-vertex $\Gamma(k, k')$

$$\Gamma_\alpha(k, k') = \sum_i \sigma_i \, \tilde{u}_i(k) \, \tilde{v}_i(k') \tag{52}$$

$$\tilde{u}_i(k) = \sum_j \, v_j^\Phi(k) \, \frac{\langle u_j^\Phi(k), U_i(k) \rangle}{\sigma_j^\Phi},$$

$$\tilde{v}_i(k) = \sum_j \, \frac{\langle V_i(k), v_j^\Phi(k) \rangle}{\sigma_j^\Phi} \, u_j^\Phi(k) \,.$$

[2]The set of basis-functions $\{\mathcal{B}\}$ can be freely chosen, since the DCA$^+$ is not dependent on the choice of the basis-functions. Usually, one uses cubic Hermite splines [27].

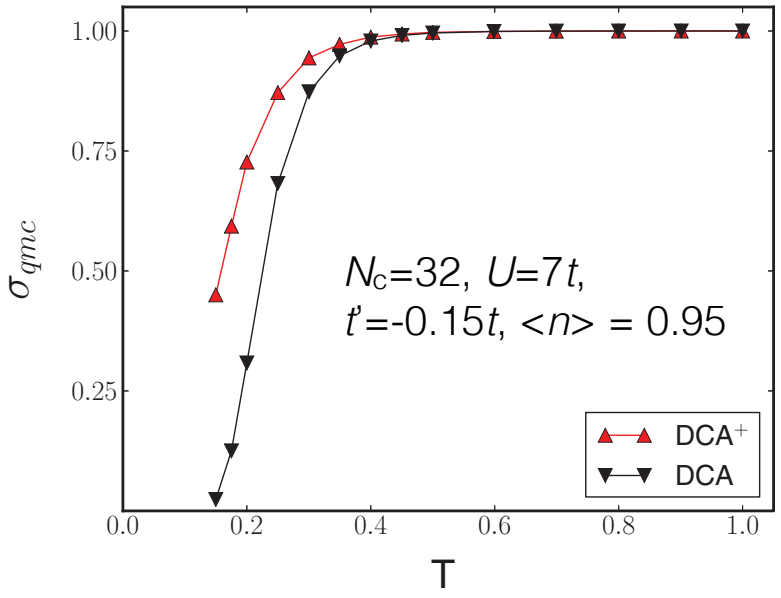

Fig. 10: DCA$^+$ reduction of the sign problem: *The average QMC sign compared between DCA and DCA$^+$ for a 32-site cluster with $U = 7\,t$, $t' = -0.15\,t$ and $\langle n \rangle = 0.95$. The DCA$^+$ algorithm reduces the sign problem of the DCA further. Figure reproduced from Ref. [5].*

Here, $\langle a, b \rangle$ represents the usual dot-product between vectors a and b. One generally finds that the singular values of the Φ-matrix decay rapidly. Note that this set of equations has a stable solution only if the expansion coefficients $\langle u_j^\Phi(k), U_i(k) \rangle$ and $\langle V_i(k), v_j^\Phi(k) \rangle$ decay faster than the singular values. For numerical reasons, one generally imposes an upper bound to the inverse of the singular values σ_i^Φ. Due to the statistical noise of the Monte Carlo solution, the expansion coefficients may become small, but usually not zero. To stabilize the inversion, it is helpful to convert $1/\sigma_i^\Phi$ to the value $\min\{1/\epsilon, 1/\sigma_i^\Phi\}$, where ϵ is a small but finite number. In this way, all components are taken into account [5].

3.3 Reduction of the QMC sign problem

As discussed in Sec. 2.3, DCA QMC calculations have a much less severe sign problem than finite-size QMC calculations. Fig. 10 compares the QMC sign between DCA$^+$ and DCA calculations. One sees that the DCA$^+$ further reduces the sign problem (at a given low temperature it has a larger average sign). Intuitively, this can be understood in the following way: Empirically, it is known that the sign problem gets worse when the strength of the correlations increases. The step discontinuities in the $\boldsymbol{k}$-dependence of the DCA self-energy lead to artificial long-range correlations in real space. The smooth momentum dependence of the DCA$^+$ lattice self-energy removes these artificial long-range correlations, and this is believed to reduce the sign problem. In any case, with the larger average sign in the DCA$^+$ it is possible to study the physics of fermionic systems in larger clusters, at lower temperatures or larger interaction strength.

4 Applications to the 2D Hubbard model

DCA simulations of the single-band Hubbard model [1,28,29] have found behavior that is reminiscent of what is observed in the cuprate high-temperature superconductors. In the paramagnetic state, the low-energy spin excitations become suppressed below the crossover temperature T^*, and a pseudogap opens in the density of states at the chemical potential. At lower temperatures, one finds a finite-temperature transition to antiferromagnetic long-range order at low doping, while at larger doping, an instability to a $d_{x^2-y^2}$-wave superconducting state is found.

4.1 Antiferromagnetism

The finite-temperature antiferromagnetic instability found in DCA calculations of the Hubbard model is an apparent contradiction to the Mermin-Wagner theorem [30], which demands that such a transition is suppressed to zero temperature. In the DCA, it results from the fact that long-range (small q) fluctuations beyond the cluster size, which suppress ordering, are neglected and replaced by a mean-field. With increasing cluster size, however, the DCA progressively includes longer-ranged fluctuations while retaining some mean-field character. Larger clusters are thus expected to systematically drive the Néel temperature to zero and hence recover the Mermin-Wagner theorem in the infinite-cluster-size limit. $T_{\rm N}$ is the temperature at which the spin susceptibility

$$\chi_s(\boldsymbol{q}) = \int_0^\beta d\tau \, \langle T_\tau \, S^z(\boldsymbol{q},\tau) \, S^z(-\boldsymbol{q},0) \rangle \, , \tag{53}$$

diverges for $\boldsymbol{q} = (\pi,\pi)$. Here $S^z(\boldsymbol{q}) = 1/N \sum_{\boldsymbol{k}} (c^\dagger_{\boldsymbol{k}+\boldsymbol{q}\uparrow} c_{\boldsymbol{k}\uparrow} - c^\dagger_{\boldsymbol{k}+\boldsymbol{q}\downarrow} c_{\boldsymbol{k}\downarrow})$ is the z-component of the spin operator. $\chi_s(\boldsymbol{q})$ is calculated from the two-particle Green's function in the particle-hole magnetic channel, in a similar fashion as the pair-field susceptibility described in Sec. 2.4. The basic approximation is that the irreducible vertex function in the Bethe-Salpeter equation for this two-particle Green's function is replaced by the irreducible vertex function calculated in the effective cluster problem.

Fig. 11 shows DCA results for the Néel temperature $T_{\rm N}$ of a half-filled Hubbard model with $U = 8\,t$ reproduced from Ref. [31]. $T_{\rm N}$ decreases slowly with increasing cluster size N_c. This decrease can be understood from a scaling argument in which one assumes that an antiferromagnetic transition occurs when the correlation length ξ reaches the linear cluster size, i.e., $\xi(T_{\rm N}) = \sqrt{N_c}$ in 2D. Since correlations develop exponentially with decreasing temperature in 2D, i.e. $\xi(T) \sim e^{C/T}$, one obtains a logarithmic decrease of $T_{\rm N}(N_c)$ with N_c as seen in the data for $N_c > 4$. This decrease is consistent with $T_{\rm N} \to 0$ in the infinite-size cluster limit as required by the Mermin-Wagner theorem. The clusters with $N_c = 2$ and 4 are special because their coordination number is reduced from four. In these clusters, local singlet states form below a temperature of $J = 4t^2/U$ and suppress antiferromagnetism.

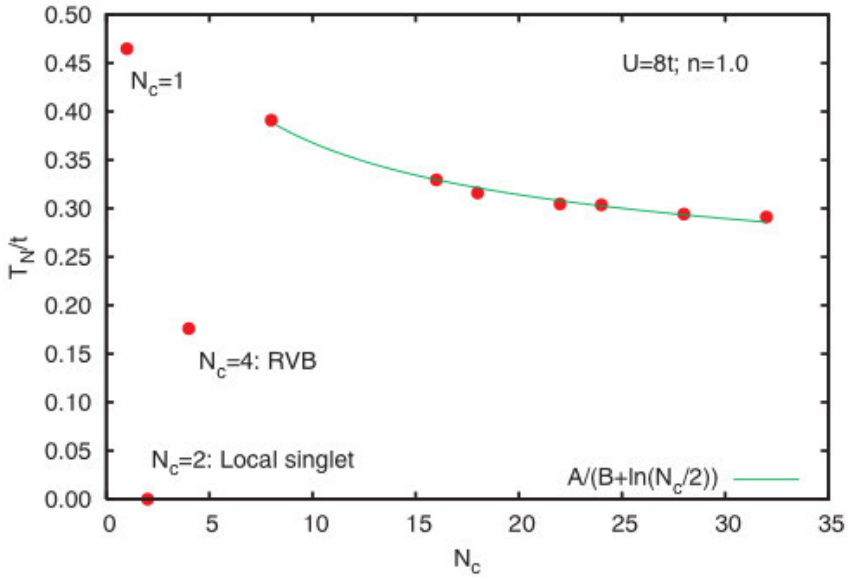

Fig. 11: DCA calculation of the Néel temperature $T_{\rm N}$ versus cluster size in a half-filled Hubbard model with U = 8t: *$T_{\rm N} \to 0$ for $N_c \to \infty$ as required by the Mermin-Wagner theorem. The solid line represents a fit to the function $A/[B + \ln(N_c)/2]$ obtained from the scaling ansatz $\xi(T_{\rm N}) = \sqrt{N_c}$. For $N_c = 2$ and 4 local singlets form in the cluster that suppress the AF state. Figure reproduced from Ref. [31].*

4.2 Pseudogap

Measurements of magnetic susceptibility and Knight shifts have found the opening of a pseudogap, a partial suppression of low energy spin fluctuations, in the underdoped cuprates [32]. ARPES experiments have found that this gap is anisotropic, opening in the anti-nodal $(\pi, 0)$ and $(0, \pi)$ regions of the Fermi surface. This state appears below a temperature T^*, which rises with decreasing hole doping as the Mott-insulating half-filled state is approached. DCA calculations of the 2D Hubbard model have found a similar pseudogap in the bulk spin susceptibility $\chi_s(\boldsymbol{q} = 0)$ [11, 33] and in calculations of the single-particle spectral weight [28, 34].

To illustrate these results, and to further compare the convergence properties between DCA and DCA$^+$, we show in Fig. 12 DCA (left panel) and DCA$^+$ results[3] (right panel) for the temperature dependence of the $\boldsymbol{q} = 0$ spin susceptibility χ_s. The DCA and DCA$^+$ results display similar behavior for $\chi_s(\boldsymbol{q} = 0, T)$ with a peak at $T^*(N_c)$ and a decrease below T^*, reflecting the opening of the pseudogap. For the DCA, however, one observes a strong cluster size dependence and poor convergence even for the largest clusters that can still be simulated before the QMC sign problem makes calculations impossible. In the DCA$^+$ results, one sees that convergence is reached much sooner. And in addition, because of the reduced sign problem, larger clusters can be reached, for which one sees that T^* is converged.

[3]For the DCA, $\chi_s(\boldsymbol{q} = 0, T)$ was determined in the same way as the $\boldsymbol{q} = (\pi, \pi)$ susceptibility in the previous section, using the same algorithm as that described for the pair-field susceptibility in Sec. 2.4, just for the magnetic spin $S = 1$ particle-hole channel instead of the particle-particle channel. For the DCA$^+$ results, the full DCA$^+$ lattice self-energy $\Sigma(\boldsymbol{k})$ was used in the Green's functions entering this formalism, but the deconvolution of the irreducible vertex function described in Sec. 3.2 was not performed. Instead this quantity was set equal to the cluster irreducible vertex function, just as in the DCA. This approximation is justified because of the weak internal $\boldsymbol{k}$ dependence of the correlations in the antiferromagnetic particle-hole channel.

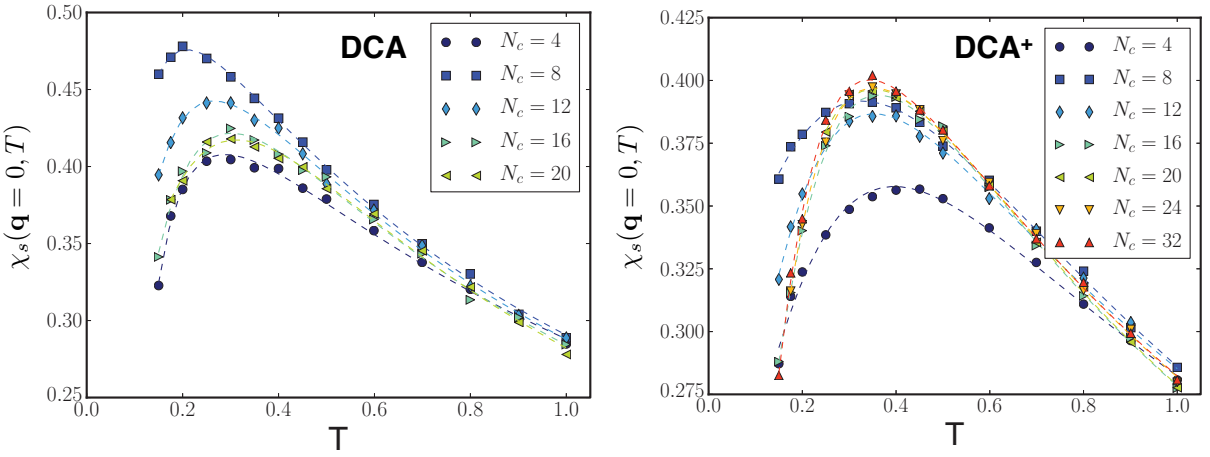

Fig. 12: Pseudogap in the uniform spin susceptibility: *DCA (left panel) and DCA$^+$ (right panel) results for the uniform spin susceptibility $\chi_s(\boldsymbol{q} = 0, T)$ versus temperature for a Hubbard model with $U = 7\,t$, $t' = -0.15\,t$ and $\langle n \rangle = 0.95$. $\chi_s(\boldsymbol{q} = 0, T)$ peaks at a temperature $T^*(N_c)$ and decreases at lower temperatures as the pseudogap opens. The DCA$^+$ converges $T^*(N_c)$ more rapidly and its reduced sign problem enables calculations at lower temperatures. Figures reproduced from Ref. [5].*

4.3 Superconductivity

DCA methods have also been used extensively to investigate the possibility and nature of superconductivity in the 2D Hubbard model [1, 21, 29, 31], because of its relevance to the cuprate high-temperature superconductors [35, 36]. Early DCA calculations used a 2×2 cluster to map out the temperature versus doping phase diagram for $U = 8\,t$ and found $d_{x^2-y^2}$-wave superconductivity over a large finite-doping region with a maximum $T_c \sim 0.08\,t$ at a filling $\langle n \rangle = 0.95$ [33]. A DCA study of larger clusters up to 26 sites was then carried out for $U = 4\,t$ and found a superconducting transition at $T_c \approx 0.023\,t$ for $\langle n \rangle = 0.9$ [31]. But convergence was poor due to the cluster shape and size dependence of the standard DCA. Recent DCA$^+$ calculations for the same parameters could reach clusters up to 52 sites, for which the results were asymptotically converged, and a finite-size scaling analysis similar to that discussed in Sec. 4.1 gave a $T_c = 0.02\,t$ [6].

As an illustration of recent progress on this issue, Fig. 13 shows the results of standard DCA and DCA$^+$ calculations for a more realistic $U = 7\,t$ and $\langle n \rangle = 0.9$ taken from Ref. [6]. The DCA$^+$ results in this figure were obtained by using a different coarse-graining [37], in which the patch function $\phi_{\boldsymbol{K}}(\boldsymbol{k})$ for a given $\boldsymbol{K}$ is finite over several intervals instead of just a single one. This leads to a further reduction of the sign problem, which is also reflected in the difference in the maximum cluster size between the DCA and DCA$^+$ results in Fig. 13. The standard DCA calculations with the usual coarse-graining are limited to only 12 sites or fewer, for this value of U, and T_c is clearly not converged. The DCA$^+$ calculations with modified coarse-graining, however, are able to reach clusters of up to 28 sites. In particular, one sees that for clusters between 12 and 26 sites, T_c changes by only 10% between different N_c, and one can estimate $T_c \approx 0.052\,t$. For $N_c = 24$ and $T = 0.05\,t$, the right panel of Fig. 13 displays the momentum dependence of the leading eigenvector $\phi_d(\boldsymbol{k}, \pi T)$ of the BSE along the diagonal from $(\pi, 0)$ to

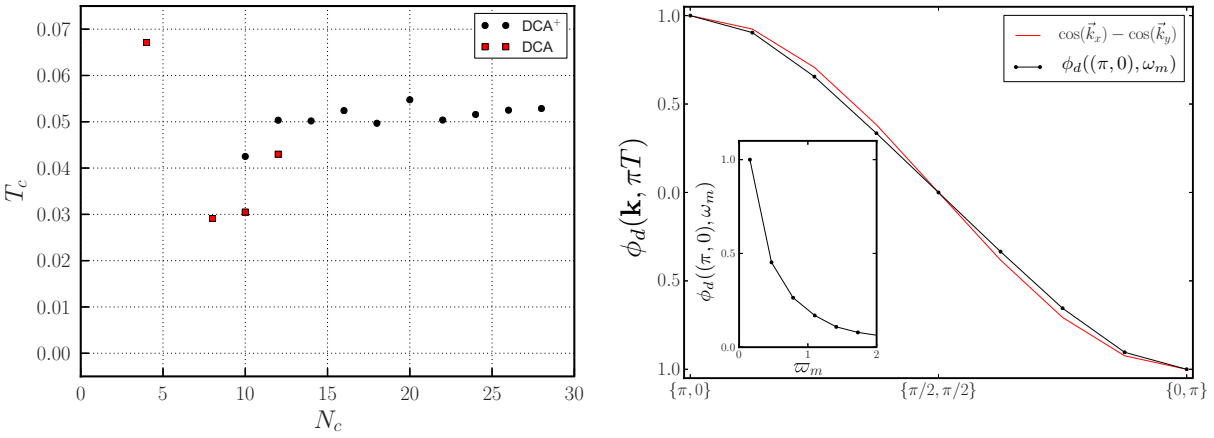

Fig. 13: Superconducting transition temperature T_c and BSE leading eigenvector of a Hubbard model with $U = 7\,t$ and $\langle n \rangle = 0.9$: *(Left panel) The QMC sign problem limits the largest accessible cluster size. DCA results (red squares) for T_c are not converged. The DCA$^+$ with modified coarse-graining (see text) allows calculations for larger clusters, for which T_c hardly changes (black circles). (Right panel) The $\boldsymbol{k}$-dependence of the leading eigenvector $\phi_d(\boldsymbol{k}, \pi T)$ of the particle-particle BSE for $T = 0.05\,t$ and $N_c = 24$ is close to $\cos k_x - \cos k_y$; its frequency dependence is plotted in the inset. Figures reproduced from Ref. [6].*

$(0, \pi)$. Compared to the coarse $\boldsymbol{K}$-dependence of the DCA result in Fig. 6, the DCA$^+$ provides information with much higher resolution in $\boldsymbol{k}$, and thus allows one to estimate deviations from the simple d-wave $\cos k_x - \cos k_y$ form factor with higher precision.

5 General discussion and concluding remarks

We have seen that the DCA approximation and its DCA$^+$ extension are quantum cluster methods that map the bulk lattice problem onto a finite-size cluster embedded in a mean-field host that is designed to represent the remaining degrees of freedom. This is achieved through a coarse-graining of the momentum space, which effectively reduces the degrees of freedom to those of a cluster, while retaining the effects of the remaining bulk degrees of freedom as a mean-field, which the cluster is coupled to. Correlations on the cluster are treated accurately using, for example, quantum Monte Carlo methods, while longer-range correlations are described on the mean-field level. Because of translational invariance of the bulk lattice, the properties of the mean-field host are calculated from the effective cluster problem in a self-consistent manner. In the DCA, the mean-field host reflects the correlations described by the cluster self-energy directly. In the DCA$^+$, in contrast, the mean-field is calculated using a lattice self-energy with continuous bulk momentum dependence that is generated from the cluster self-energy. This leads to an improved cluster shape and size dependence, and to a reduction of the sign problem in the underlying QMC cluster solver. In what follows, we give a brief discussion of several other fundamental features that are common to both the DCA and DCA$^+$ algorithms.

Nature of approximation and limitations

The basic assumption of the coarse-graining approximation in both the DCA and DCA$^+$ methods is that correlations are short-ranged so that the $\boldsymbol{k}$-dependence of the self-energy $\Sigma(\boldsymbol{k}, i\omega_n)$ and the irreducible vertex functions $\Gamma_\alpha(\boldsymbol{k}, i\omega_n, \boldsymbol{k}', \omega_{n'})$ is well approximated by a coarse grid of cluster momenta $\boldsymbol{K}$ at intervals $\Delta K = 2\pi/L_c$, where L_c is the linear cluster size. Obviously, this approximation assumes a self-energy and irreducible vertex functions that are only weakly $\boldsymbol{k}$-dependent, or equivalently, correlations that are short-ranged and do not extend beyond a length of $L_c/2$. This type of approximation is therefore expected to be appropriate for cases with significant screening, where correlations are short-ranged. It is clear that such an approximation breaks down in the proximity of classical or quantum phase transitions, where the critical behavior is governed by the long wave-length fluctuations. Since the fluctuations beyond $L_c/2$ are replaced by a mean-field, the DCA and DCA$^+$ approaches give mean-field critical behavior and possibly predict instabilities at finite temperature even when prohibited by the Mermin-Wagner theorem, as is the case, for example, for the observed finite-temperature antiferromagnetic transition in the half-filled 2D Hubbard model discussed in Sec. 4.1. The fact that instabilities occur when the correlation length extends beyond the cluster size, however, allows one to use finite-size scaling in combination with calculations on increasingly larger clusters to extrapolate to the exact infinite cluster size limit.

Causality

A particular challenge in the development of quantum cluster methods such as the DCA and DCA$^+$ has been the requirement of causality [1], i.e., that the algorithm give a self-energy with negative imaginary part, i.e. $\mathrm{Im}\, \Sigma(\boldsymbol{k}, \omega + i0^+) < 0$. For the standard DCA algorithm, it is possible to prove causality [1,3]. Hettler *et al*. also remarked [3] that the use of a simple interpolation of the cluster self-energy to generate a lattice self-energy in the coarse-graining step Eq. (11) will lead to causality violations if $\mathrm{Im}\, \Sigma_c(\boldsymbol{K}, i\omega_n)$ has a minimum somewhere in the Brillouin zone, which is generally the case. In Ref. [38], such causality violations were more fundamentally related to the "ringing" phenomenon in Fourier-analysis. To avoid these problems in the DCA, one interpolates the cluster self-energy only after the calculation is converged. The DCA$^+$ algorithm, however, is fundamentally different from a simple interpolation of the cluster self-energy. The constraint of the DCA$^+$ algorithm in Eq. (37) demands that the coarse-grained lattice self-energy $N_c/N \sum_{\boldsymbol{k}} \phi_{\boldsymbol{K}}(\boldsymbol{k}) \Sigma(\boldsymbol{k})$ is equal to the cluster self-energy $\Sigma_c(\boldsymbol{K})$. Except for very special cases, this results in a lattice self-energy $\Sigma(\boldsymbol{k})$ that is different from a simple interpolation of the cluster self-energy $\Sigma_c(\boldsymbol{K})$. The arguments for causality violations that arise when a simple interpolation is used in Refs. [3, 38] thus do not apply, and the DCA$^+$ algorithm does not necessarily violate causality. Although a rigorous proof for the causality of the DCA$^+$ is not available, violations of causality have not yet been observed in any of the applications of this method [5].

Thermodynamic consistency

Thermodynamic consistency in the Baym and Kadanoff sense [39] ensures that observables calculated from the single-particle Green's function agree with those calculated from the two-particle Green's function. For example, the pair-field susceptibility may be determined from the two-particle formalism described in Sec. 2.4. Alternatively, one may extend the single-particle formalism to allow for calculations in the superconducting phase by introducing an anomalous Green's function $F_{ij}(\tau) = -\langle T_\tau\, c_{i\uparrow}(\tau) c_{j\downarrow}(0)\rangle$. The s-wave pair-field susceptibility, for example, is then obtained from $P_s = \partial \Delta_s / \partial \Psi|_{\Psi=0}$, where Ψ is the applied pair-field and $\Delta_s = T/N \sum_{\boldsymbol{k},\omega_n} F(\boldsymbol{k}, i\omega_n)$. Thermodynamically consistent algorithms will give the same result, irrespective of whether P_s is calculated on the single-particle level or whether it is calculated on the two-particle level. An algorithm is thermodynamically consistent if it is self-consistent and if the two-particle irreducible vertex function Γ is related to the single-particle self-energy through $\Gamma = \delta\Sigma[G]/\delta G$. This is the case in the DCA where both Σ and Γ are obtained as derivatives of the same Baym-Kadanoff Φ-functional (see Appendix and [1]) and approximated by their respective cluster quantities Σ_c and Γ_c. In the DCA$^+$, it is important that the relation between Γ and Γ_c is consistent with the relation between Σ and Σ_c. In both cases, the cluster quantities are related to their lattice counterparts by a coarse-graining relation, as seen from Eqs. (37) and (45), and it was shown in Ref. [6] that these relations indeed satisfy $\Gamma = \delta\Sigma[G]/\delta G$. Accordingly, the DCA$^+$ algorithm is thermodynamically consistent if a similar procedure is used to extract the lattice quantities.

Conclusions

In this lecture we have tried to communicate that the DCA and DCA$^+$ approximations are powerful theoretical approaches that enable reliable and, in certain cases, controlled studies of the rich phenomenology in systems dominated by strong electronic correlations. They are non-perturbative in nature and, in conjunction with numerically exact QMC cluster solvers, provide an unbiased tool to understand the physics in these systems. They enable the calculation of static and dynamic single-particle and two-particle correlation functions and thus allow for the determination of various experimentally accessible observables, such as those related to photoemission, transport, magnetism, and superconductivity. Despite the reduction in complexity, the solution of the effective cluster problem remains a challenging task, and its complexity increases rapidly as the number of cluster degrees of freedom increases. Hence these methods have been applied almost exclusively to low-energy effective descriptions of the full many-body problem, such as the single-band Hubbard model discussed in this lecture. Applications to more complex multi-orbital models are required when the specifics of certain materials need to be included. This can be achieved along the lines of the local density approximation + DMFT approach, where the models studied by DMFT or DCA are parametrized by electronic structure calculations. While this remains an important and challenging task, the progress in [40–42] demonstrates that calculations along these lines are within reach.

Acknowledgments

I would like to acknowledge discussions with E. Gull, M. Jarrell, J. Keller, A. Macridin, S. Okamoto, T. Pruschke, D.J. Scalapino, T.C. Schulthess and P. Staar that have led to a deeper understanding and appreciation of the formalisms presented in this lecture. Support from the Center for Nanophase Materials Sciences and resources of the Oak Ridge Leadership Computing Facility, which are DOE Office of Science User Facilities, are also greatly acknowledged.

Appendix

A DCA and DCA$^+$ as self-energy functional approximations

General methods may be derived from the Green's function based formalism of Luttinger and Ward [43] and Baym and Kadanoff [39], where the grand potential

$$\Omega[\boldsymbol{G}] = \mathrm{Tr}\ln[-\boldsymbol{G}] - \mathrm{Tr}\left[(\boldsymbol{G}_0^{-1} - \boldsymbol{G}^{-1})\,\boldsymbol{G}\right] + \Phi[\boldsymbol{G}, \boldsymbol{U}] \tag{54}$$

is expressed in terms of the single-particle Green's function $\boldsymbol{G}$.[4] Here, $\Phi[\boldsymbol{G}]$ is the so-called Baym-Kadanoff functional described in Ref. [39]. The self-energy $\boldsymbol{\Sigma}$ is obtained from the functional derivative of $\Phi[\boldsymbol{G}]$ with respect to $\boldsymbol{G}$

$$\boldsymbol{\Sigma} = \frac{\delta\Phi[\boldsymbol{G}]}{\delta\boldsymbol{G}} \tag{55}$$

and is related to the Green's function via the Dyson equation (8)

$$\boldsymbol{G}^{-1} = \boldsymbol{G}_0^{-1} - \boldsymbol{\Sigma}\,. \tag{56}$$

These two relations imply that the free energy Ω is stationary with respect to $\boldsymbol{G}$, i.e.

$$\frac{\delta\Omega[\boldsymbol{G}]}{\delta\boldsymbol{G}} = 0\,. \tag{57}$$

In principle, the exact Green's function $\boldsymbol{G}$ and self-energy $\boldsymbol{\Sigma}$ can be determined from the self-consistent solution of Eqs. (55) and (56). However, since the functional $\Phi[\boldsymbol{G}]$ is usually unknown, an approximation is required that replaces the exact $\Phi[\boldsymbol{G}]$ by a known or computable functional. Conserving approximations replace the exact $\Phi[\boldsymbol{G}]$ by an approximate functional, which considers certain sub-classes of diagrams that can be summed up analytically and that are thought to capture the dominant physics. This generally results in a weak coupling approximation such as second-order perturbation theory or the fluctuation exchange approximation [44]. These approaches usually fail, however, when the interaction U gets larger than several times the hopping t.

DCA

The DCA therefore takes a different approach. From Eq. (12), one sees that fundamentally the DCA is an approximation of the self-energy where

$$\Sigma^{\mathrm{DCA}}(\boldsymbol{k}) \simeq \sum_{\boldsymbol{K}} \Phi_{\boldsymbol{K}}(\boldsymbol{k})\,\Sigma_c(\boldsymbol{K})\,. \tag{58}$$

To proceed, it is therefore convenient to follow the work of Potthoff [45] and Okamoto [38] and express the grand potential in terms of the self-energy instead of the Green's function

$$\Omega[\boldsymbol{\Sigma}] = \mathrm{Tr}\ln\left[-(\boldsymbol{G}_0^{-1} - \boldsymbol{\Sigma})\right] - (\mathcal{L}\Phi)[\boldsymbol{\Sigma}]\,. \tag{59}$$

[4] Here we have used a matrix equation for the Green's functions $\boldsymbol{G}$ and $\boldsymbol{G}_0$ and the trace Tr sums over momenta $\boldsymbol{k}$ and frequencies ω_n.

Here, the functional $(\mathcal{L}\Phi)[\boldsymbol{\Sigma}]$ is obtained from $\Phi[\boldsymbol{G}]$ through a Legendre transform

$$(\mathcal{L}\Phi)[\boldsymbol{\Sigma}] = \Phi - \mathrm{Tr}[\boldsymbol{\Sigma}\boldsymbol{G}]\,. \tag{60}$$

At stationarity, i.e. $\delta\Omega[\boldsymbol{\Sigma}]/\delta\boldsymbol{\Sigma} = 0$, one again obtains the usual Dyson equation $[\boldsymbol{G}_0^{-1} - \boldsymbol{\Sigma}]^{-1} = \boldsymbol{G}$, where $\boldsymbol{G} = -\delta(\mathcal{L}\Phi)[\boldsymbol{\Sigma}]/\delta\boldsymbol{\Sigma}$. However, just as $\Phi[\boldsymbol{G}]$ is unknown, the functional $(\mathcal{L}\Phi)[\boldsymbol{\Sigma}]$ is generally unknown. Instead of replacing the functional by a low order weak coupling approximation, the DCA keeps the same functional but reduces the complexity by replacing the exact self-energy $\Sigma(\boldsymbol{k})$ by the approximation in Eq. (58), i.e. $\Sigma(\boldsymbol{k}) \simeq \Sigma^{DCA}(\boldsymbol{k}) = \sum_{\boldsymbol{K}} \phi_{\boldsymbol{K}}(\boldsymbol{k})\, \Sigma_c(\boldsymbol{K})$. This replacement reduces the degrees of freedom over which the functional is evaluated to those of a finite-size cluster,

$$(\mathcal{L}\Phi)[\boldsymbol{\Sigma}_c] = \Phi - \frac{N}{N_c}\sum_{\boldsymbol{K}} \mathrm{Tr}[\Sigma_c(\boldsymbol{K})\, G_c(\boldsymbol{K})] \tag{61}$$

with

$$G_c(\boldsymbol{K}) = \frac{N_c}{N}\sum_{\boldsymbol{k}} \phi_{\boldsymbol{K}}(\boldsymbol{k})\, G(\boldsymbol{k}) = \frac{N_c}{N}\sum_{\boldsymbol{k}} \phi_{\boldsymbol{K}}(\boldsymbol{k})\, \frac{1}{G_0^{-1}(\boldsymbol{k}) - \Sigma^{DCA}(\boldsymbol{k})}\,. \tag{62}$$

Relation (62) implies that the parameters of the effective cluster problem are fixed by the requirement that the cluster Green's function $\boldsymbol{G}_c$ is equal to the coarse-grained lattice Green's function on the right-hand side. Using the relation $\delta(\mathcal{L}\Phi)[\boldsymbol{\Sigma}_c]/\delta\boldsymbol{\Sigma}_c = -N/N_c\, \boldsymbol{G}_c$ together with
$\delta\Sigma^{DCA}(\boldsymbol{k})/\delta\Sigma_c(\boldsymbol{K}) = \phi_{\boldsymbol{K}}(\boldsymbol{k})$, it is straightforward to show that the relation (62) implies that the DCA approximation for the grand potential

$$\Omega^{DCA}[\boldsymbol{\Sigma}_c] = \mathrm{Tr}\ln\left[-(\boldsymbol{G}_0^{-1} - \boldsymbol{\Sigma}^{DCA})\right] + \Phi - \sum_{\boldsymbol{K}} \mathrm{Tr}[\Sigma_c(\boldsymbol{K}) G_c(\boldsymbol{K})]\,. \tag{63}$$

is stationary, i.e. $\delta\Omega[\boldsymbol{\Sigma}_c]/\delta\Sigma_c(\boldsymbol{K}) = 0$.

DCA$^+$

Just like in the DCA, the DCA$^+$ approach replaces the self-energy in the functional $(\mathcal{L}\Phi)[\boldsymbol{\Sigma}]$ by the piecewise-constant cluster approximation $\sum_{\boldsymbol{K}} \phi_{\boldsymbol{K}}(\boldsymbol{k})\, \Sigma_c(\boldsymbol{K})$ to limit the degrees of freedom over which this term is calculated to those of a finite-size cluster. But in contrast to the DCA, this replacement is not made in the first $\mathrm{Tr}\ln[-(\boldsymbol{G}_0^{-1} - \boldsymbol{\Sigma})]$ term of the grand-potential $\Omega[\boldsymbol{\Sigma}]$. Instead, here one retains the full lattice self-energy $\boldsymbol{\Sigma}(\boldsymbol{k})$ to give the DCA$^+$ approximation

$$\Omega^{DCA^+}[\boldsymbol{\Sigma}] = \mathrm{Tr}\ \ln\left[-(\boldsymbol{G}_0^{-1} - \boldsymbol{\Sigma})\right] + \Phi - \frac{N}{N_c}\sum_{\boldsymbol{K}} \mathrm{Tr}[\Sigma_c(\boldsymbol{K})\, G_c(\boldsymbol{K})]\,. \tag{64}$$

Note that in contrast to the DCA where the grand potential reduces to a functional of the cluster self-energy, i.e. $\Omega[\boldsymbol{\Sigma}] \to \Omega^{DCA}[\boldsymbol{\Sigma}_c]$, here, the grand potential remains a functional of the lattice self-energy $\Sigma(\boldsymbol{k})$, which enters in the first term. Then again, one can ask for stationarity of the grand potential. When the cluster self-energy $\boldsymbol{\Sigma}_c$ is related to the lattice self-energy $\boldsymbol{\Sigma}$ through the DCA$^+$ constraint

$$\Sigma_c(\boldsymbol{K}) = \frac{N_c}{N}\sum_{\boldsymbol{k}} \phi_{\boldsymbol{K}}(\boldsymbol{k})\, \Sigma(\boldsymbol{k})\,, \tag{65}$$

one obtains from $\delta\Omega^{DCA^+}[\Sigma(\boldsymbol{k})]/\delta\Sigma(\boldsymbol{k}) = 0$

$$\left[G_0^{-1}(\boldsymbol{k}) - \Sigma(\boldsymbol{k})\right]^{-1} = \sum_{\boldsymbol{K}} \phi_{\boldsymbol{K}}(\boldsymbol{k})\, G_c(\boldsymbol{K})\,. \tag{66}$$

To derive the right-hand side we have used $\delta\Sigma_c(\boldsymbol{K})/\delta\Sigma(\boldsymbol{k}) = N_c/N\,\phi_{\boldsymbol{K}}(\boldsymbol{k})$ according to Eq. (65). Using the identity Eq. (36) and multiplying both sides with $N_c/N\sum_{\boldsymbol{k}}\phi_{\boldsymbol{K}}(\boldsymbol{k})$ results in the DCA$^+$ coarse-graining equation Eq. (38), i.e.

$$G_c(\boldsymbol{K}) = \frac{N_c}{N}\sum_{\boldsymbol{k}} \phi_{\boldsymbol{K}}(\boldsymbol{k})\,\frac{1}{G_0^{-1}(\boldsymbol{k}) - \Sigma(\boldsymbol{k})}\,. \tag{67}$$

This proves that the DCA$^+$ algorithm, just like the DCA algorithm gives results for the self-energy and the Green's function that correspond at self-consistency to a stationary solution of the DCA$^+$ grand potential.

References

[1] T. Maier, M. Jarrell, T. Pruschke, and M. Hettler, Rev. Mod. Phys. **77**, 1027 (2005)

[2] M.H. Hettler, A.N. Tahvildar-Zadeh, M. Jarrell, T. Pruschke, and H.R. Krishnamurthy, Phys. Rev. B **58**, R7475 (1998)

[3] M. Hettler, M. Mukherjee, M. Jarrell, and H. Krishnamurthy, Phys. Rev. B **61**, 12739 (2000)

[4] T. Maier, M. Jarrell, T. Pruschke, and J. Keller, Eur. Phys. J. B **13**, 613 (2000)

[5] P. Staar, T. Maier, and T.C. Schulthess, Phys. Rev. B **88**, 115101 (2013)

[6] P. Staar, T. Maier, and T.C. Schulthess, Phys. Rev. B **89**, 195133 (2014)

[7] J. Hubbard, Proc. Royal. Soc. London **276**, 238 (1963)

[8] R.R. dos Santos, Braz. J. Phys. **33**, 36 (2003)

[9] E. Dagotto, Rev. Mod. Phys. **66**, 763 (1994)

[10] J. Hirsch and R. Fye, Phys. Rev. Lett. **56**, 2521 (1986)

[11] M. Jarrell, T. Maier, C. Huscroft, and S. Moukouri, Phys. Rev. B **64**, 195130 (2001)

[12] E. Gull, A.J. Millis, A.I. Lichtenstein, A.N. Rubtsov, M. Troyer, and P. Werner, Rev. Mod. Phys. **83**, 349 (2011)

[13] E. Gull, P. Werner, O. Parcollet, and M. Troyer, Europhys. Lett. **82**, 57003 (2008)

[14] S. Rombouts, K. Heyde, and N. Jachowicz, Phys. Rev. Lett. **82**, 4155 (1999)

[15] E. Gull, P. Staar, S. Fuchs, P. Nukala, M. Summers, T. Pruschke, T.C. Schulthess, and T.A. Maier, Phys. Rev. B **83**, 075122 (2011)

[16] P. Staar, T.A. Maier, and T.C. Schulthess, J. Phys.: Conf. Series **402**, 012015 (2012)

[17] A. Georges, W. Krauth, and M. Rozenberg, Rev. Mod. Phys. **68**, 13 (1996)

[18] S. Moukouri and M. Jarrell, Phys. Rev. Lett. **87**, 167010 (2001)

[19] M. Troyer and U. Wiese, Phys. Rev. Lett. **94**, 170201 (2005)

[20] N. Bulut, D.J. Scalapino, and S.R. White, Phys. Rev. B **47**, 14599 (1993)

[21] T.A. Maier, M.S. Jarrell, and D.J. Scalapino, Phys. Rev. Lett. **96**, 047005 (2006)

[22] T.A. Maier, M. Jarrell, and D. Scalapino, Phys. Rev. B **74**, 094513 (2006)

[23] T.D. Stanescu and G. Kotliar, Phys. Rev. B **74**, 125110 (2006)

[24] N. Marzari, A.A. Mostofi, J.R. Yates, I. Souza, and D. Vanderbilt, Rev. Mod. Phys. **84**, 1419 (2012)

[25] W.H. Richardson, J. Opt. Soc. Am. **62**, 55 (1972)

[26] L.B. Lucy, Astron. J. **79**, 745 (1974)

[27] R. Keys, IEEE Trans. Acoust. Speech **29**, 1153 (1981)

[28] E. Gull, M. Ferrero, O. Parcollet, A. Georges, and A. Millis, Phys. Rev. B **82**, 155101 (2010)

[29] E. Gull, O. Parcollet, and A.J. Millis, Phys. Rev. Lett. **110**, 216405 (2013)

[30] N. Mermin and H. Wagner, Phys. Rev. Lett. **17**, 1133 (1966)

[31] T.A. Maier, M. Jarrell, T.C. Schulthess, P.R.C. Kent, and J.B. White, Phys. Rev. Lett. **95**, 237001 (2005)

[32] T. Timusk and B. Statt, Rep. Prog. Phys. **62**, 61 (1999)

[33] M. Jarrell, T. Maier, M.H. Hettler, and A. Tahvildarzadeh, Europhys. Lett. **56**, 563 (2001)

[34] C. Huscroft, M. Jarrell, T. Maier, S. Moukouri, and A. Tahvildarzadeh, Phys. Rev. Lett. **86**, 139 (2001)

[35] P.W. Anderson, Science **235**, 1196 (1987)

[36] F. Zhang and T. Rice, Phys. Rev. B **41**, 7243 (1990)

[37] P. Staar, M. Jiang, U. Hähner, T. Maier, and T. Schulthess, in preparation (2015)

[38] S. Okamoto, A.J. Millis, H. Monien, and A. Fuhrmann, Phys. Rev. B **68**, 195121 (2003)

[39] G. Baym and L. Kadanoff, Phys. Rev. **124**, 287 (1961)

[40] A.I. Poteryaev, A.I. Lichtenstein, and G. Kotliar, Phys. Rev. Lett. **93**, 086401 (2004)

[41] P.R.C. Kent, T. Saha-Dasgupta, O. Jepsen, O.K. Andersen, A. Macridin, T. Maier, M. Jarrell, and T.C. Schulthess, Phys. Rev. B **78**, 035132 (2008)

[42] Y. Nomura, S. Sakai, and R. Arita, Phys. Rev. B **89**, 195146 (2014)

[43] J. Luttinger and J. Ward, Phys. Rev. **118**, 1417 (1960)

[44] N. Bickers, D. Scalapino, and S. White, Phys. Rev. Lett. **62**, 961 (1989)

[45] M. Potthoff, Eur. Phys. J. B **32**, 429 (2003)